File from Steve Long's computer dated 08/16/02 12:01pm named "ORNL_Failure_Criterion_08_14_02.pdf"

ORNL/NRC/LTR-

Contract Program or Project Title:	Heavy-Section Steel Technology (HSST) Program
Subject of this Document:	Stochastic Failure Model for the Davis-Besse RPV Head
Type of Document:	Letter Report
Authors:	P. T. Williams B. R. Bass
Date of Document:	August 2002
Responsible NRC Individual and NRC Office or Division	M. T. Kirk Division of Engineering Technology Office of Nuclear Regulatory Research

Prepared for the
U. S. Nuclear Regulatory Commission
Washington, D.C. 20555-0001
Under Interagency Agreement DOE 1886-N653-3Y
NRC JCN No. Y6533

OAK RIDGE NATIONAL LABORATORY
Oak Ridge, Tennessee 37831-8056
managed and operated by
UT-Battelle, LLC for the
U. S. DEPARTMENT OF ENERGY
under Contract No. DE-AC05-00OR22725

ORNL Y/2

ORNL/NRC/LTR-

Stochastic Failure Model for the Davis-Besse RPV Head

P. T. Williams
B. R. Bass

Oak Ridge National Laboratory
Oak Ridge, Tennessee

Manuscript Completed – August 2002
Date Published –

Prepared for the
U.S. Nuclear Regulatory Commission
Office of Nuclear Regulatory Research
Under Interagency Agreement DOE 1886-N653-3Y

NRC JCN No. Y6533

OAK RIDGE NATIONAL LABORATORY
Oak Ridge, Tennessee 37831-8063
managed and operated by
UT-Battelle, LLC for the
U. S. DEPARTMENT OF ENERGY
under Contract No. DE-AC05-00OR22725

CAUTION

This document has not been given final patent clearance and is for internal use only. If this document is to be given public release, it must be cleared through the site Technical Information Office, which will see that the proper patent and technical information reviews are completed in accordance with the policies of Oak Ridge National Laboratory and UT-Battelle, LLC.

Stochastic Failure Model for the Davis-Besse RPV Head

P. T. Williams and B. R. Bass
Oak Ridge National Laboratory
P. O. Box 2009
Oak Ridge, TN, 37831-8056

Abstract

The development of several stochastic models is described in this report in which the uncertainties associated with predictions of burst pressure for circular diaphragms using computational or analytical methods are estimated. It is postulated that the trends seen in predicting the burst pressure with nine experimental disk-burst tests (using materials, geometries, and pressure badings relevant to the Davis-Besse analysis) will be representative of the computational predictions of the burst pressure in the Davis-Besse wastage area problem. Given a computational prediction of burst pressure for a specific configuration of the wastage area, the scaled stochastic models provide an estimate of the cumulative probability that the true burst pressure will be less than any given service pressure.

The stochastic models were developed from the following technical bases:

(1) *experimental data* obtained during disk-burst tests with loadings, geometries, and materials relevant to the Davis-Besse pressure loading, wastage-area footprint, and cladding,

(2) nonlinear, large-deformation, elastic-plastic *discrete-element analyses* of the disk-burst tests,

(3) nonlinear, finite-strain, elastic-plastic *finite-element analyses* performed for the current study, and

(4) a *theoretical criterion* for plastic instability in a circular diaphragm under pressure loading, applied to the disk-burst tests.

Among the twenty-seven continuous distributions investigated, six passed all of the heuristic and *Goodness of Fit* tests applied in the analysis. The six distributions, ranked in relative order, are: (1) Log-Laplace, (2) Beta, (3) Gamma, (4) Normal, (5) Random Walk, and (6) Inverse Gaussian (Wald).

As an example application, estimates are provided for a bounding calculation of the "as-found" Davis-Besse wastage area. The bounding calculation predicted a burst pressure of 6.65 ksi which has a cumulative probability of failure of 0.158 using the Log-Laplace model. The Log-Laplace model also estimates a cumulative probability of failure of 4.14×10^{-7} at the operating pressure of 2.165 ksi and 2.15×10^{-6} at the set-point pressure of 2.5 ksi. Using all six distributions, the average probability of failure is 6.91×10^{-8} at 2.165 ksi, 3.60×10^{-7} at 2.5 ksi, and 0.2155 at 6.65 ksi.

1. Introduction

1.1. Objective

This report presents stochastic models of failure for the stainless steel cladding in the wastage area of the Davis-Besse Nuclear Power Station reactor pressure vessel (RPV) head. For a given internal pressure, the statistical models provide estimates of the cumulative probability (*probability of nonexceedance*) that the exposed cladding will have failed at a lower pressure. The failure mode addressed by this model is *incipient tensile plastic instability* (i.e., plastic collapse) of the cladding.

1.2. Background

The following was taken from ref. [1].

> On February 16, 2002, the Davis-Besse facility began a refueling outage that included inspection of the vessel head penetration (VHP) nozzles, which focused on the inspection of control rod drive mechanism (CRDM) nozzles, in accordance with the licensee's commitments to NRC Bulletin 2001-01, "Circumferential Cracking of Reactor Pressure Vessel Head Penetration Nozzles," which was issued on August 3, 2001. These inspections identified axial indications in three CRDM nozzles, which had resulted in pressure boundary leakage. Specifically, these indications were identified in CRDM nozzles 1, 2, and 3, which are located near the center of the RPV head. ... Upon completing the boric acid removal on March 7, 2002, the licensee conducted a visual examination of the area, which identified a large cavity in the RPV head on the downhill side of CRDM nozzle 3. Followup characterization by the ultrasonic testing indicated wastage of the low alloy steel RPV head material adjacent to the nozzle. The wastage area was found to extend approximately 5 inches downhill on the RPV head from the penetration for CRDM nozzle 3, with a width of approximately 4 to 5 inches at its widest part.

See Fig. 1. for a photograph of the Davis-Besse RPV, a schematic of a typical nuclear power reactor, and a sketch and photographs of the wastage area.

1.3. Scope

In support of the investigation by the United States Nuclear Regulatory Commission's (NRC) Office of Nuclear Regulatory Research, the Heavy-Section Steel Technology Program at Oak Ridge National Laboratory has developed statistical models for a specific failure mode for the exposed stainless steel cladding in the cavity of the Davis-Besse RPV head. Section 2 reviews the technical bases employed in the development of the models; Section 3 presents the details of the stochastic models; Section 4 demonstrates an application of the top-ranked Log-Laplace model to the results of a bounding calculation for the "as found" condition of the wastage area; and Section 5 provides a summary and conclusions.

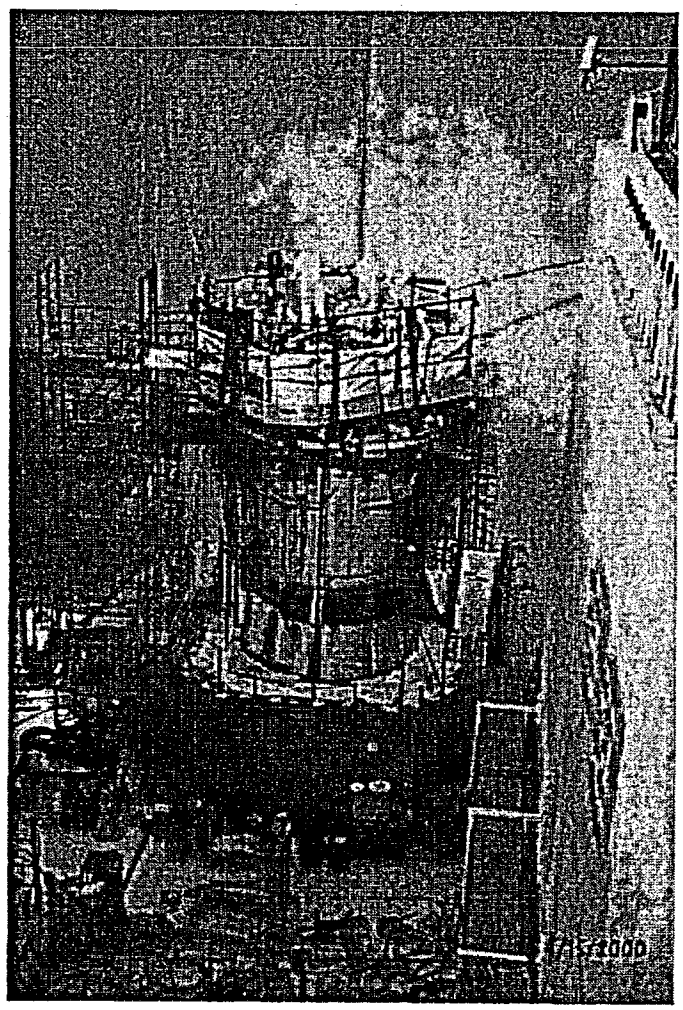

Davis Besse Reactor Vessel Head Degradation Head Cutaway View

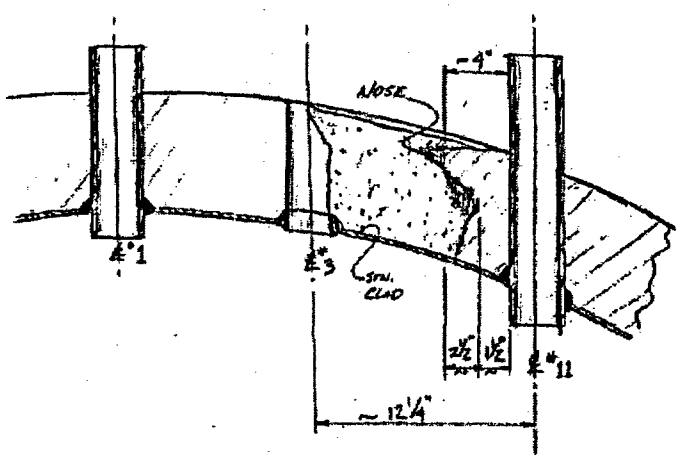

The above figure shows the Davis Besse reactor vessel head degradation between nozzle #3 and nozzle #11. This sketch was provided to the NRC by the Licensee.

Fig. 1. (a) Davis-Besse Nuclear Power Station RPV and (b) sketch of RPV head degradation.

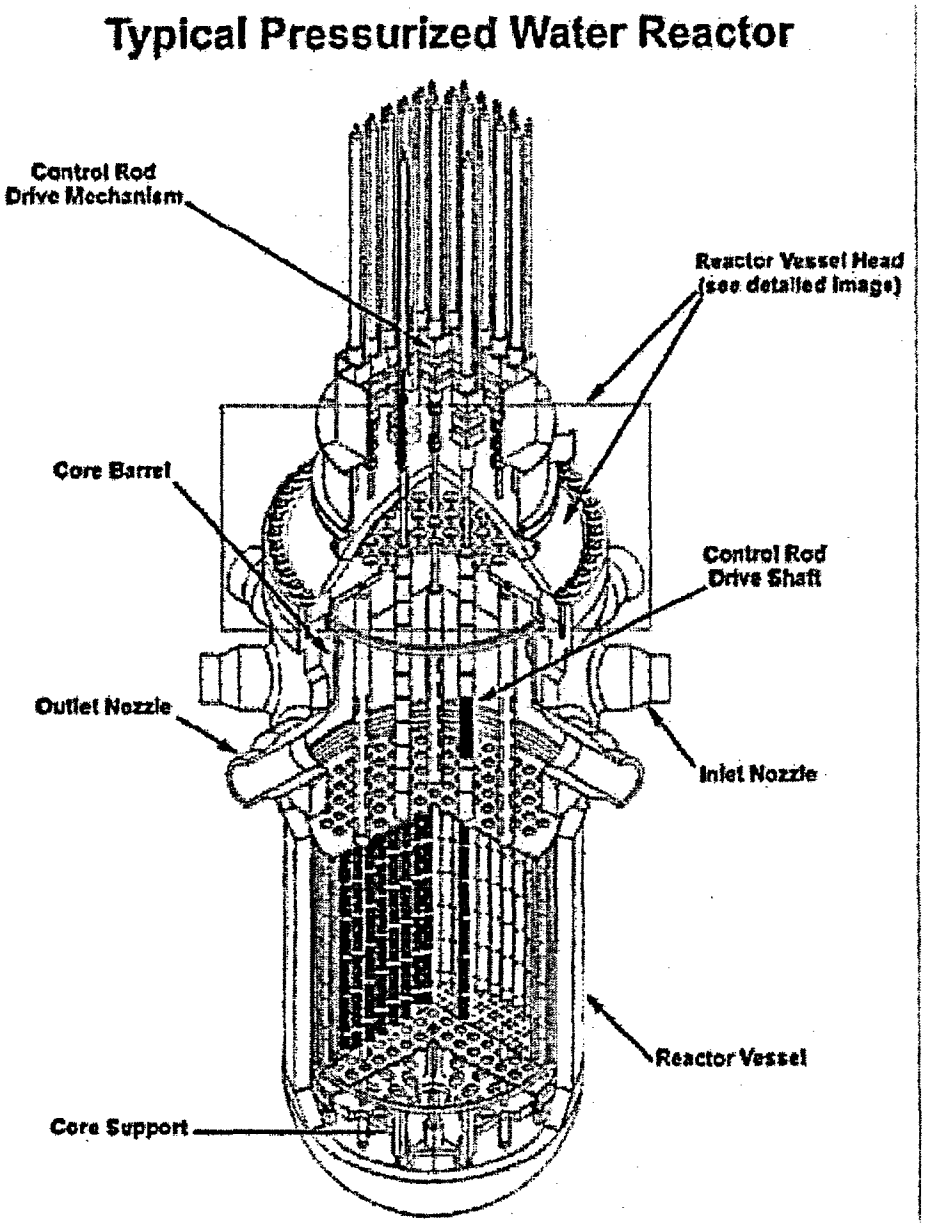

Fig. 1 (continued) (c) schematic of a typical nuclear power reactor showing the relationship of the CRDM nozzles to the RPV head.

Fig. 1. (continued) (d) photographs of the wastage area with Nozzle 3 removed.

2. Technical Bases

The technical bases employed in the construction of the stochastic models are:

(1) *experimental data* obtained during disk-burst tests reported by Riccardella [2] with loadings, geometries, and materials relevant to the Davis-Besse pressure loading, wastage-area footprint, and cladding,

(2) nonlinear, large-deformation, elastic-plastic *discrete-element analyses* of the disk-burst tests also reported in [2] (GAPL-3 discrete-element code[3]),

(3) nonlinear, finite-strain, elastic-plastic *finite-element analyses* performed for the current study (ABAQUS finite-element code[4]) of the nine disk-burst test specimens reported in [2], and

(4) a *theoretical criterion* for plastic instability in a circular diaphragm under pressure loading, due to Hill [5] (as cited in [6]), applied to the disk-burst tests.

2.1. Experimental – Disk-Burst Tests

In the early 1970s, constrained disk-burst tests were carried out under the sponsorship of the *PVRC Subcommittee on Effective Utilization of Yield Strength* [7]. This test program employed a range of materials and specimen geometries that were relevant to components in a nuclear power plant steam supply system[1]. The geometries of the three test specimens analyzed in [2] are shown in Fig. 2, the test matrix is shown in Table 1, and the properties of the three materials are presented in Table 2. The nine disk-burst tests produced three center failures and six edge failures over a range of burst pressures from 3.75 to 15 ksi as shown in Table 1.

Table 1. Test Matrix for Disk-burst Tests [2]

Test Number	Material	Geometry	Fillet Radius (in.)	Diaphragm Thickness (in.)	Effective Diaphragm Radius (in.)	Experimental Results: Burst Pressure (ksi)	Experimental Results: Location of Failure
1	SS 304	A	0.375	0.250	2.625	15	Edge
2		B	0.125	0.125	2.875	6.8	Center
3		C	0.375	0.125	2.625	7.7	Center
4	A533B	A	0.375	0.250	2.625	11	Edge
5		B	0.125	0.125	2.875	5.3	Edge
6		C	0.375	0.125	2.625	6.7	Center
7	ABS-C	A	0.375	0.250	2.625	9.8	Edge
8		B	0.125	0.125	2.875	3.75	Edge
9		C	0.375	0.125	2.625	4.94	Edge

[1] The three materials are representative of reactor core support structures and piping, the reactor pressure vessel, and plant component support structures [2].

Table 2. Property Data for Materials in Disk-burst Tests [2]

Material	Yield Strength 0.2% offset (ksi)	Ultimate Strength (ksi)	Strain at Ultimate (-)	True Stress 0.2% offset (ksi)	True Ultimate Stress (ksi)	Log Strain at Ultimate (-)	Power Law Fit* K (ksi)	Power Law Fit* n (-)
SS304	34	84	0.54	34.07	129.36	0.432	162.41	0.27
A-533B	74	96	0.17	74.15	112.32	0.157	139.41	0.12
ABS-C	39	64	0.31	39.08	83.84	0.270	105.20	0.17

*The power-law parameters in Table 2 were fitted for the current study where $\bar{\sigma} = K\bar{\varepsilon}^n$ and $\bar{\sigma}$, $\bar{\varepsilon}$ are the effective true stress and effective total true strain, respectively.

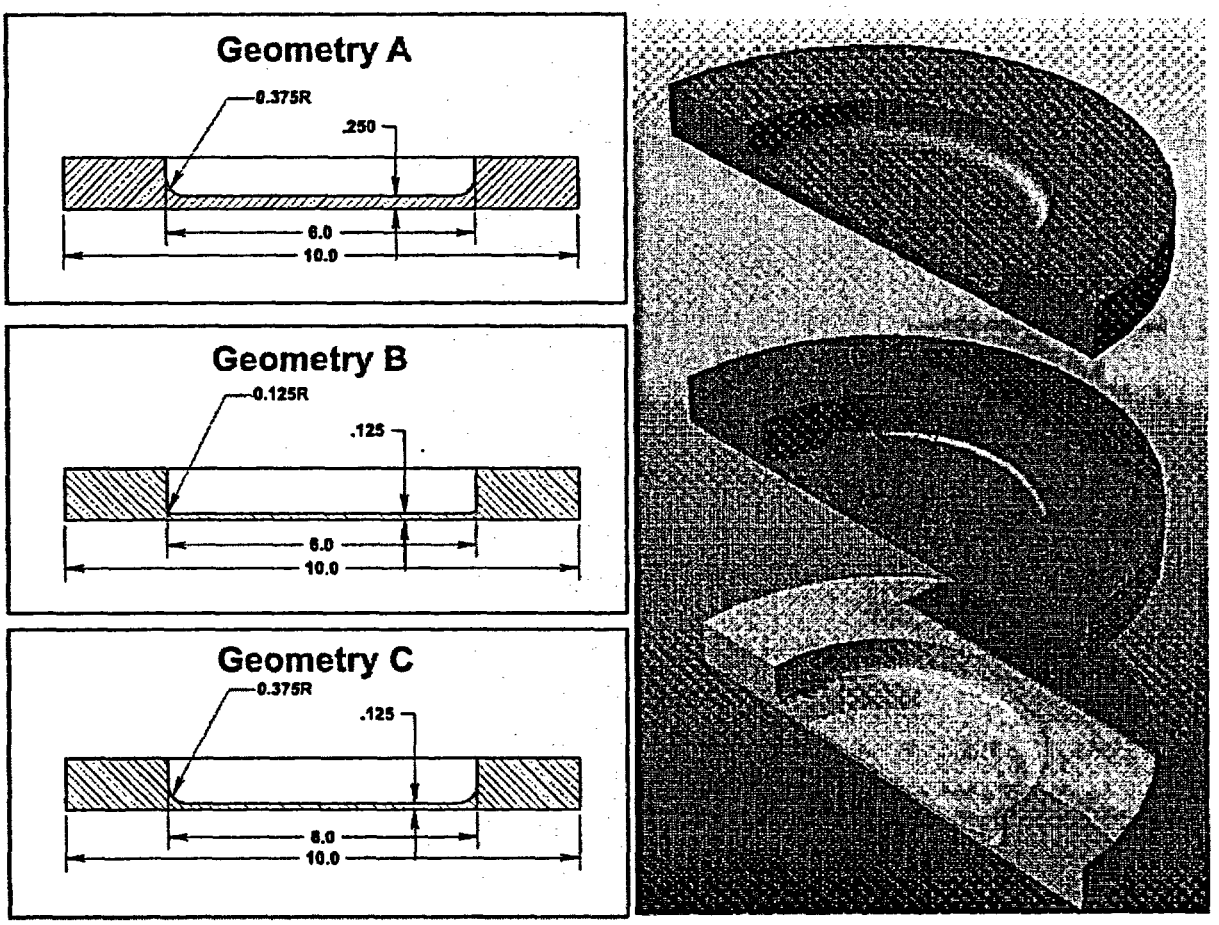

Fig. 2. Geometric descriptions of the three disk-burst specimens used in [1] (all dimensions are inches). Images on the right are Photoworks®-rendered views of ½-symmetry solid models of the three specimens.

2.2. Computational – Axisymmetric Discrete-Element and Finite-Element Models

The results of a computational study were presented in [2] in which the nine tests were simulated using the GAPL-3 computer code [3]. GAPL-3 applied the *discrete-element* method using a two-layered system of elements: one layer for the strain-displacement field and a second layer for the stress field to perform an elasto-plastic large-deformation analysis of stresses, strains, loads, and displacements of thin plates or axisymmetric shells with pressure loading. At each incremental load step, the code iterated to resolve both geometric and material nonlinearities, thus establishing a condition of static equilibrium. The GAPL-3 code did not account for the reduction in thickness of the diaphragm with increasing load, and, therefore, was unable to demonstrate the "tailing up" of the experimental center-deflection histories. As discussed in [2], the thin-shell approximation of the GAPL-3 code is not strictly valid in the fillet region. The GAPL-3 model did include a plastic-hinge type of strain redistribution, but the strain concentration effect due to the fillet radius was not accounted for, since the predicted strain distribution in the cross-section of the fillet was linear by assumption. These approximations in the analysis were driven by the limitations of the computer resources available at the time of the study in 1972.

The current study reanalyzed all nine disk-burst tests using the ABAQUS [4] finite-element code. With current computing power, many of the simplifying assumptions required in 1972 could be removed to provide a more detailed analysis. The fundamental assumptions made in the current study are:

(1) the material is assumed to be homogenous and isotropic before and throughout plastic deformation;

(2) the material is assumed to be free of pre-existing defects;

(3) the volume of the material undergoing plastic deformation is assumed to be constant (i.e., incompressible with a Poisson's ratio of 0.5);

(4) the hydrostatic component of the stress tensor has no effect on yielding; and

(5) the plastic deformation follows incremental J_2 flow theory (Mises yield criterion) with its associated flow rule (Levy-Mises) and isotropic strain hardening.

The finite-element meshes shown in Fig. 3 were developed using 8-node quadratic, axisymmetric, solid elements with reduced integration (ABAQUS element type CAX8R). The material property data given in Table 2 were used to fit power-law constitutive models for the plastic region of the three materials (see Fig. 4). The analyses applied a nonlinear finite-strain procedure with an incrementally increasing pressure load applied from zero up to the load at which numerical instabilities caused ABAQUS to abort the execution.

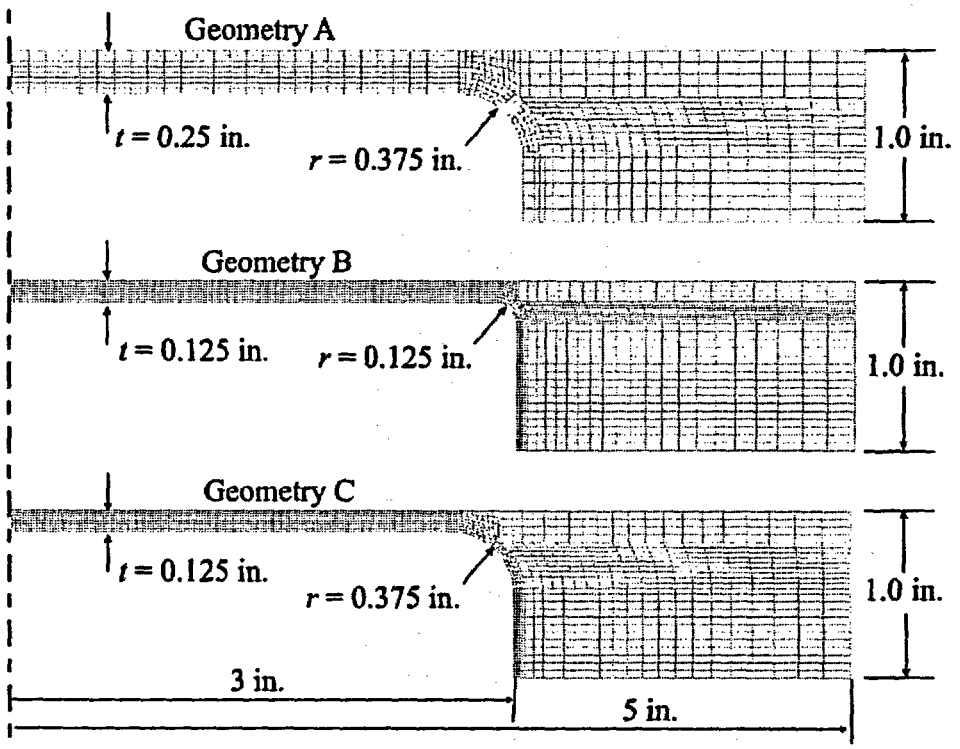

Fig. 3. Axisymmetric finite-element meshes used in the analyses of disk-burst tests reported in [2]. Quadratic 8-node axisymmetric (CAX8R) elements with reduced integration were used in a nonlinear finite-strain elastic-plastic analysis of the three disk-burst geometries with three materials.

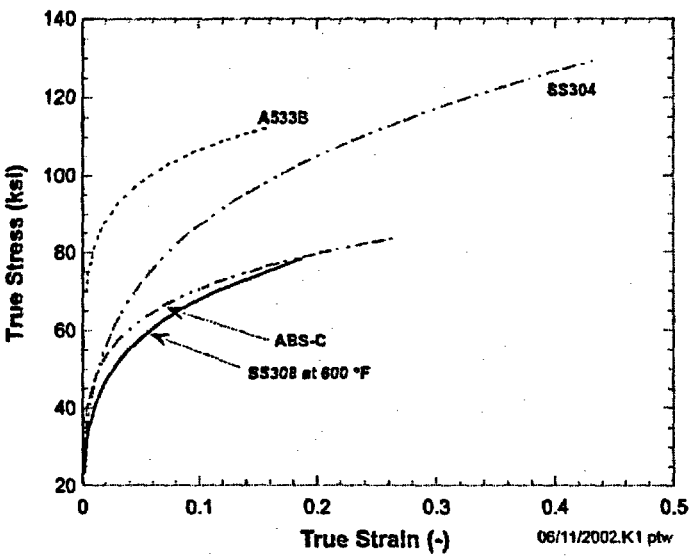

Fig. 4. True stress vs true strain curves of the three materials used in the disk-burst tests compared to SS308 at 600 °F. These three test material curves were developed using a power-law strain-hardening model fitted to yield and ultimate strength/strain data for each material given in [2]. (See Table 2).

2.3. Theory – Hill's Plastic Instability Theory

A plastic instability theory due to Hill [5] for a pressurized circular diaphragm constrained at the edges is presented in [6]. Figure 5 shows the geometry of the diaphragm, both undeformed and deformed, along with the nomenclature used in the development of the theory.

The geometry of deformation is assumed to be a spherical dome or bulge of radius, R. The undeformed ring element (defined by its position, width, and thickness, $(r_0, \delta r_0, h_0)$, respectively) is assumed to deform to an axisymmetric shell element with surface length, δL, deformed thickness, h, radial position, r, and angle ϕ. The nonuniform thickness of the dome reaches its minimum at the pole with polar height H. For a spherical coordinate system with its origin at the center of the dome, the principal strains for the thin-shell (i.e., the strains are assumed constant through the thickness) element are

$$\varepsilon_\theta = \ln\left(\frac{r}{r_0}\right);\ \varepsilon_\phi = \ln\left(\frac{\delta L}{\delta r_0}\right);\ \varepsilon_h = \ln\left(\frac{h}{h_0}\right) \tag{1}$$

A geometric relationship exists between the radius and chord of a circle such that

$$R = \frac{H^2 + a^2}{2H} \tag{2}$$

where a is the effective radius of the undeformed diaphragm. Using Eqs. (1) - (2) and the geometry shown in Fig. 5, ref. [6] derives the following relations for the meridional, ε_ϕ, and hoop, ε_θ, strains at any point on the spherical bulge

$$\varepsilon_\phi(z \mid H, a) = \varepsilon_\theta(z \mid H, a) = \ln\left[1 + \left(\frac{z\,H}{a^2}\right)\right] \tag{3}$$

where the geometric parameter z is shown in Fig. 5. Applying the constant volume assumption, i.e., $\varepsilon_\phi + \varepsilon_\theta + \varepsilon_h = 0$, produces the following equation for the radial ("thickness") strain

$$\varepsilon_h(z \mid H, a) = -2\varepsilon_\phi(z \mid H, a) = \ln\left[\frac{1}{1 + \left(zH/a^2\right)}\right]^2 \tag{4}$$

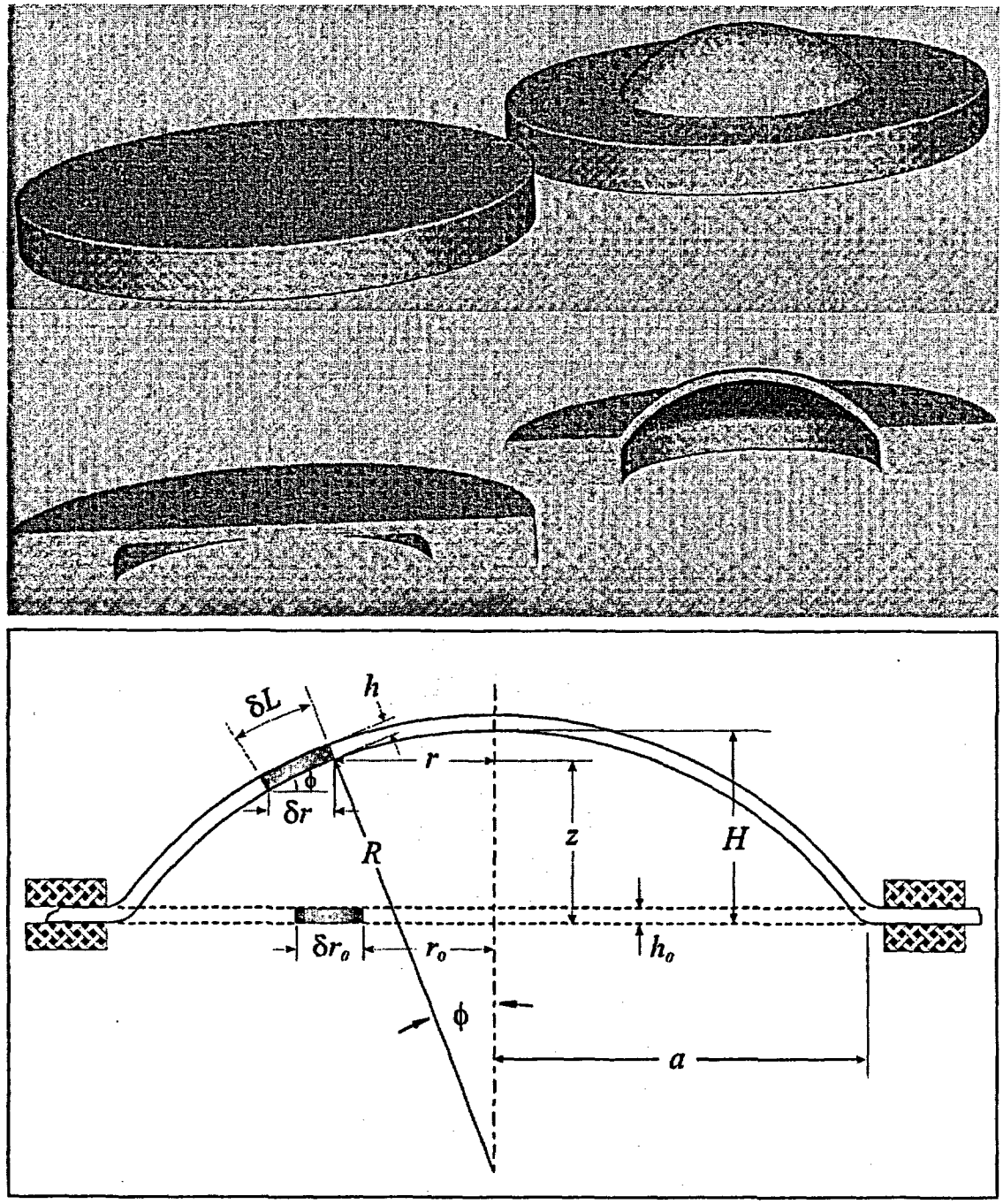

Fig. 5. Spherical geometry of deformation assumed in Hill's [5] plastic instability theory.

The effective strain then becomes

$$\bar{\varepsilon}(\varepsilon_\phi,\varepsilon_\theta,\varepsilon_h)\equiv\sqrt{\frac{2}{3}}\sqrt{(\varepsilon_\phi-\varepsilon_\theta)^2+(\varepsilon_\phi-\varepsilon_h)^2+(\varepsilon_\theta-\varepsilon_h)^2}=-\varepsilon_h(z\,|\,H,a)=2\ln\left[1+\left(\frac{z\,H}{a^2}\right)\right] \tag{5}$$

The maximum radial strain, therefore, occurs at the pole of the spherical bulge. Applying the thin-walled assumption (which is not made in the computational finite-element model) for an axisymmetric shell element, the equilibrium relation between the meridional, σ_ϕ, and hoop, σ_θ, membrane stresses and the internal pressure, p_i, loading is

$$\frac{\sigma_\phi}{R_\phi}+\frac{\sigma_\theta}{R_\theta}=\frac{p_i}{h} \tag{6}$$

For a spherical dome, $R_\theta=R_\phi=R$, and a state of equibiaxial stress is assumed to prevail near the pole of the dome with the principal stresses being

$$\sigma_\phi=\sigma_\theta=\frac{p_i R}{2h};\ \sigma_r=0 \tag{7}$$

and the effective stress, $\bar{\sigma}=\frac{1}{\sqrt{2}}\sqrt{(\sigma_\phi-\sigma_\theta)^2+(\sigma_\phi-\sigma_r)^2+(\sigma_\theta-\sigma_r)^2}$, is

$$\bar{\sigma}=\sigma_\phi=\sigma_\theta=\frac{p_i R}{2h} \tag{8}$$

To establish an instability criterion, a surface can be constructed in pressure, effective stress, and deformation/strain space by expressing Eq. (8) as a total differential of the form

$$\begin{aligned} Rp_i &= 2h\bar{\sigma} \\ Rdp_i+p_i dR &= 2hd\bar{\sigma}+2\bar{\sigma}dh \\ \frac{dp_i}{p_i} &= \frac{d\bar{\sigma}}{\bar{\sigma}}+\frac{dh}{h}-\frac{dR}{R} \end{aligned} \tag{9}$$

An unstable condition exists at a point of maximum pressure on the surface where $dp_i=0$. The condition is unstable because any perturbation from this position always involves a reduction in load (pressure), even in a rising stress field. The instability criterion for a deformed bulge of radius R is, therefore, established by the following relation between stress and the deformed geometry for any point on the dome

$$\frac{d\bar{\sigma}}{\bar{\sigma}} = \frac{dR}{R} - \frac{dh}{h} \tag{10}$$

or in terms of effective strain

$$\frac{1}{\bar{\sigma}}\frac{d\bar{\sigma}}{d\bar{\varepsilon}} = 1 + \frac{1}{R}\frac{dR}{d\bar{\varepsilon}} \tag{11}$$

If the instability condition is attained, it will first occur at the point of maximum effective strain at the top of the dome (at $z = H$) such that Eq. (11) can be stated as

$$\frac{1}{\bar{\sigma}}\frac{d\bar{\sigma}}{d\bar{\varepsilon}} = \frac{3}{2} - \frac{1}{4}\left(\frac{2}{\bar{\varepsilon}}\right)\left(1 + \frac{\bar{\varepsilon}}{2}\right) \tag{12}$$

Applying a power-law constitutive form to relate effective stress to effective strain in the plastic region,

$$\bar{\sigma} = K\,\bar{\varepsilon}^{n} \ , \tag{13}$$

the effective strain at instability is, after a great deal of algebraic manipulation,

$$\bar{\varepsilon}_{crit} = \frac{4}{11}(2n+1) \tag{14}$$

where n is the power-law exponent in the constitutive equation, Eq. (13).

For a given material and diaphragm geometry (n, a, h_0), the pressure at the instability condition (i.e., the burst pressure) can be determined by the following procedure:

- Calculate the effective critical strain. $\bar{\varepsilon}_{crit} = \frac{4}{11}(2n+1)$
- Calculate the corresponding effective critical stress. $\bar{\sigma}_{crit} = K\,\bar{\varepsilon}^{n}$
- Calculate the critical thickness. $h_{crit} = h_0 \exp(-\bar{\varepsilon}_{crit})$
- Calculate the polar height at the critical condition. $H_{crit} = a\sqrt{\exp\left(\frac{\bar{\varepsilon}_{crit}}{2}\right)-1}$
- Calculate the corresponding bulge curvature radius. $R_{crit} = \frac{H_{crit}^2 + a^2}{2H_{crit}}$
- Finally, calculate the predicted burst pressure. $p_{burst} = \frac{2h_{crit}\bar{\sigma}_{crit}}{R_{crit}}$

An alternative instability criterion was developed by Chakrabarty[8] which was based on a Tresca yield surface. The critical effective strain was found to be

$$\bar{\varepsilon}_{crit} = \frac{2(2-n)(1+2n)}{11-4n} \tag{15}$$

3. Stochastic Model Development

3.1. Computational and Theoretical Model Results

Computational results using the GAPL-3 code were presented in [2]. Converged solutions were obtained for eight of the nine tests. Comparison of experimental and computational centerline deflections showed good agreement for the eight converged cases. In the nonconverged case (ABS-C, geometry C), some difficulty was reported in getting convergence at high pressures. In all cases the experimental data showed a "tailing up" as the pressure approached burst pressure, which the computational model was unable to capture. In general, the prediction of the burst pressure for the eight converged cases showed good agreement with the experimentally-determined burst pressures. Defining α as the ratio of the experimental burst pressure to the computationally-predicted burst pressure, the mean for α was 1.19 with a standard error for the mean of ± 0.0484 and a standard deviation for the sample of 0.137.

The finite-element models using ABAQUS were able to obtain burst pressures for all nine tests, where the *predicted burst pressure* is defined as the pressure at which a breakdown occurs in the numerical procedure, causing the run to abort. For a nonlinear, finite-strain, static load step, ABAQUS uses automatic sizing of the load increment to maintain numerical stability. The number of iterations needed to find a converged solution for a load increment varies depending on the degree of nonlinearity in the system. If the solution has not converged within 16 iterations or if the solution appears to diverge, ABAQUS abandons the increment and starts again with the increment size set to 25% of its previous value. An attempt is then made at finding a converged solution with this smaller load increment. If the increment still fails to converge, ABAQUS reduces the increment size again. ABAQUS allows a maximum of five cutbacks in an increment before aborting the analysis. Therefore, ABAQUS will attempt a total of 96 iterations with six increments sizes before abandoning the solution. The initial load size for the failing increment was typically already very small due to difficulties in convergence with the previous and final successfully-converged load increment.

Equivalent plastic strain contours are shown in Fig. 4 for the geometry A (ABS-C carbon steel) specimen (Test No. 7) at the point of numerical instability. The experimental burst pressure for this specimen was 9.8 ksi, and numerical instability of the solution occurred at approximately 9.05 ksi, for an $\alpha = 1.083$. Highly localized plastic straining can be observed near the fillet, thus predicting an edge failure for this specimen which did in fact fail at its edge.

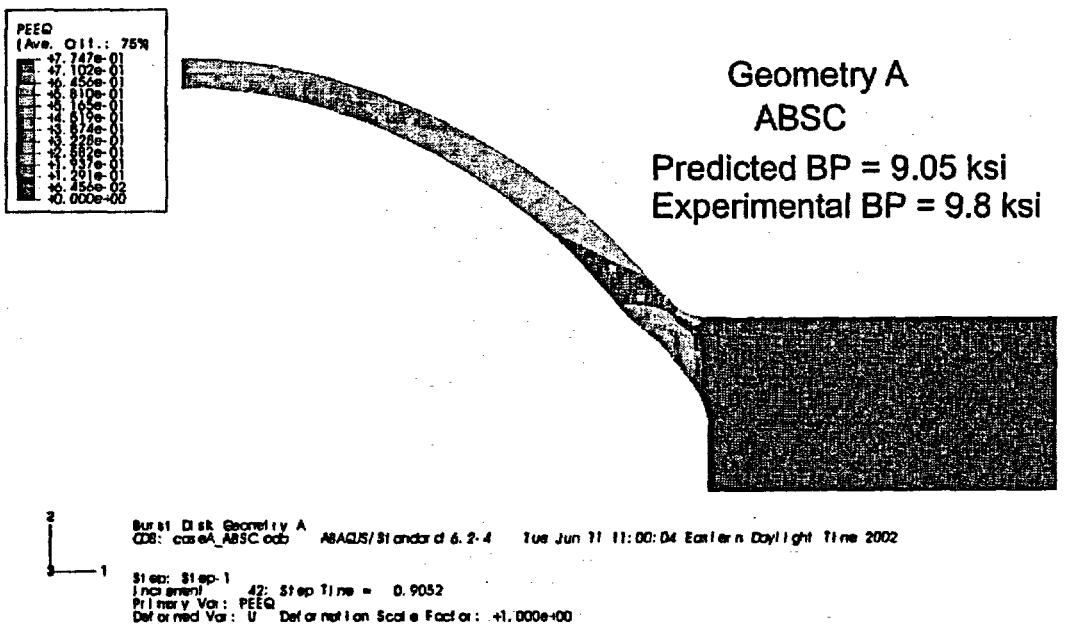

(a)

Ref. P. C. Riccardella, "Elasto-Plastic Analysis of Constrained Disk Burst Tests," ASME Paper No. 72-PVP-12, *ASME Pressure Vessels and Piping Conference*, New Orleans, LA, September 17-21, 1972.

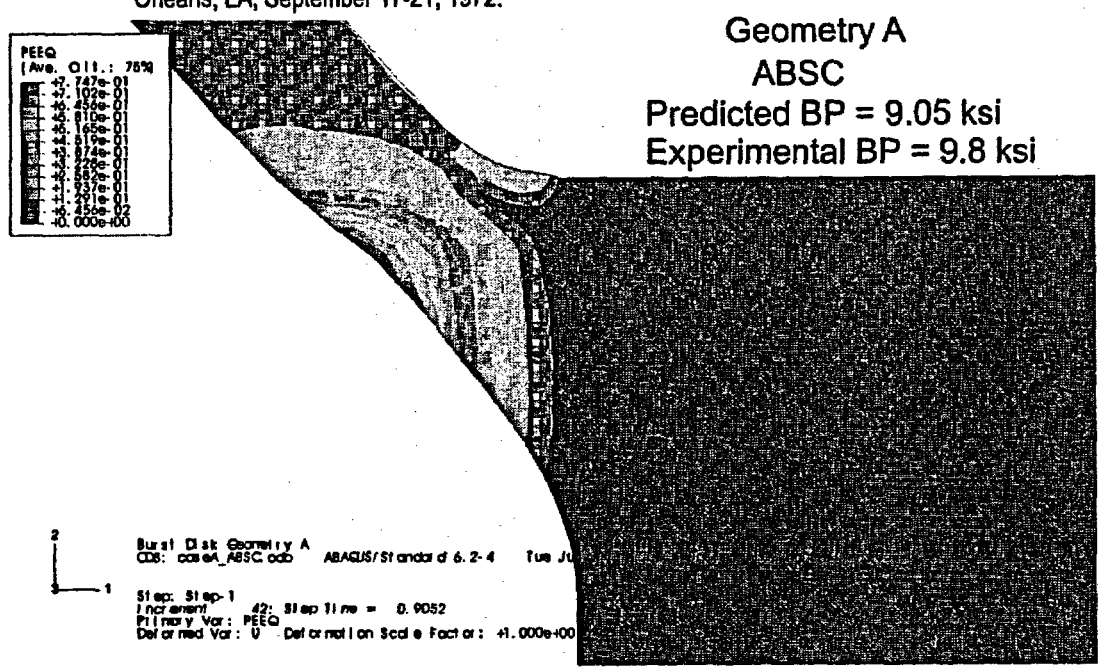

(b)

Fig. 4. Equivalent plastic strain contours for the Geometry A (ABS-C carbon steel) specimen at the point of numerical instability. Highly localized plastic straining provides a precondition for plastic collapse at the edge of the specimen. (ABAQUS analysis results)

Figure 5 compares the predicted centerline deflection load histories with the experimentally-observed deflections at failure (estimated from Figs. 3 and 4 in [2]). The "tailing up" of the experimental deflection curves near the point of failure is predicted by the model, indicating that the computational simulations are capturing the final localized "necking" of the diaphragm. For the nine ABAQUS predictions, the mean for α was 1.055 with a standard error for the mean of ±0.0331 and a standard deviation for the sample of 0.0993.

The results of applying Hill's failure criterion are presented in Table 3. The mean for α was 1.058 with a standard error for the mean of ±0.0374 and a standard deviation for the sample of 0.1123. The calculations were repeated using the theoretical critical strain of Chakrabarty and Alexander [8], Eq. (15), with the resulting burst pressures being essentially identical to those given in Table 3.

Table 3. Application of Hill's Instability Theory to Nine Disk-burst Tests

Test	K (ksi)	n	a (in.)	h_0 (in.)	ε_{crit}	H_{crit} (in.)	R_{crit} (in.)	σ_{crit} (ksi)	h_{crit} (in.)	P_{burst} (ksi)	$P_{burst(exp)}$ (ksi)	α
1	162.41	0.27	2.625	0.250	0.561	1.493	3.054	138.84	0.1427	12.98	15	1.156
2	162.41	0.27	2.875	0.125	0.561	1.635	3.345	138.84	0.0714	5.92	6.8	1.148
3	162.41	0.27	2.625	0.125	0.561	1.493	3.054	138.84	0.0714	6.49	7.7	1.187
4	139.41	0.12	2.625	0.250	0.449	1.316	3.276	126.96	0.1596	12.37	11	0.889
5	139.41	0.12	2.875	0.125	0.449	1.441	3.588	126.96	0.0798	5.65	5.3	0.938
6	139.41	0.12	2.625	0.125	0.449	1.316	3.276	126.96	0.0798	6.19	6.7	1.083
7	105.20	0.17	2.625	0.250	0.490	1.383	3.183	92.95	0.1532	8.95	9.8	1.095
8	105.20	0.17	2.875	0.125	0.490	1.514	3.486	92.95	0.0766	4.08	3.75	0.918
9	105.20	0.17	2.625	0.125	0.490	1.383	3.183	92.95	0.0766	4.47	4.94	1.104

A summary of all 26 burst pressure predictions is given in Table 4. Combining the 26 cases into a single sample gives a mean for α of 1.098 with a standard error for the mean of ±0.0251 and a standard deviation for the sample of 0.1281. Even though Hill's theory is applicable only for center failures, the good agreement between the experiments (including those that failed at the edges) suggests that, for the edge-failure cases, the specimens were also close to a condition of plastic collapse at the center when they failed first at the edge.

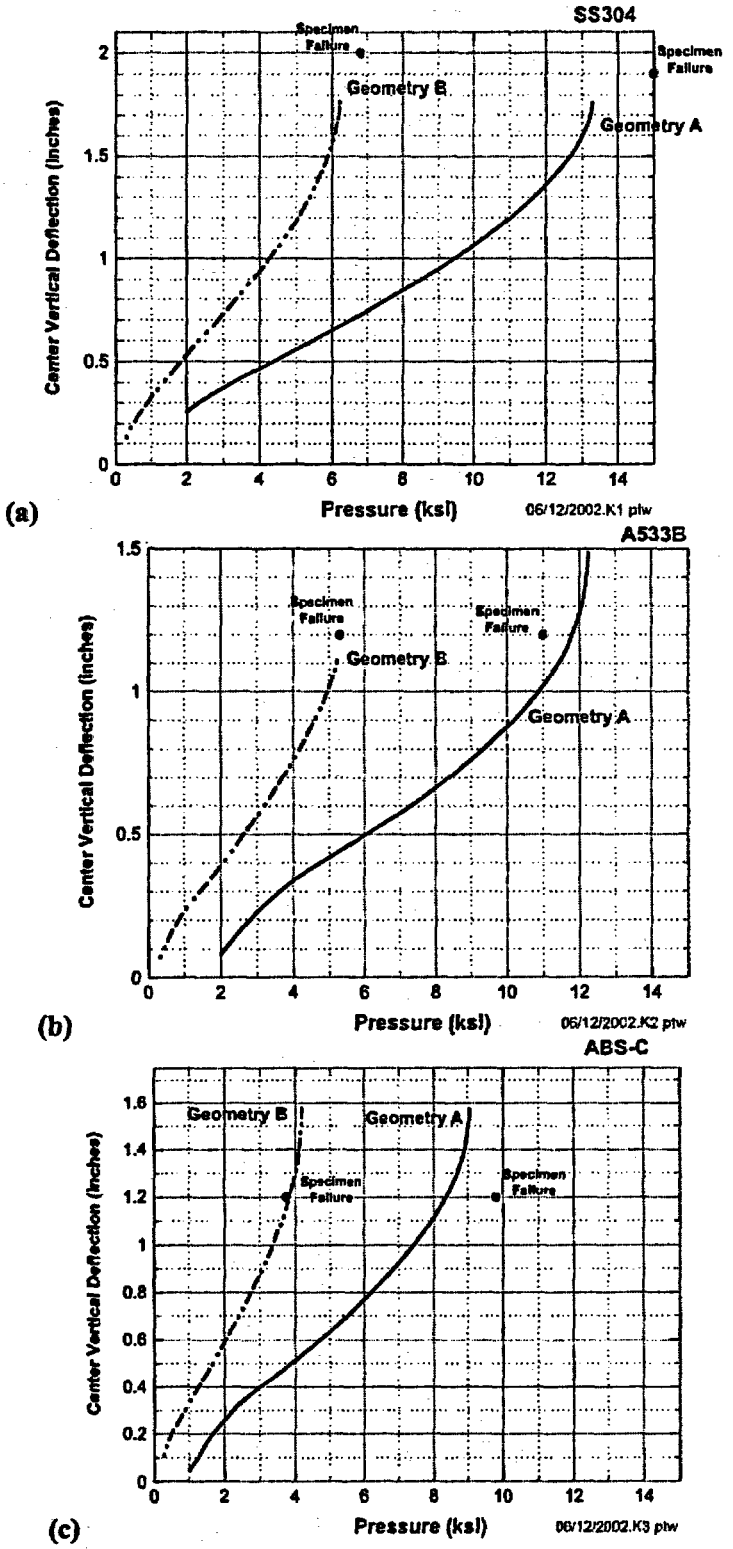

Fig. 5. Comparison of experimental centerline vertical deflections at failure to ABAQUS FEM vertical deflection histories at the center of the Geometry A and B specimens for (a) SS 304, (b) A533-B, and (c) ABS-C materials, and

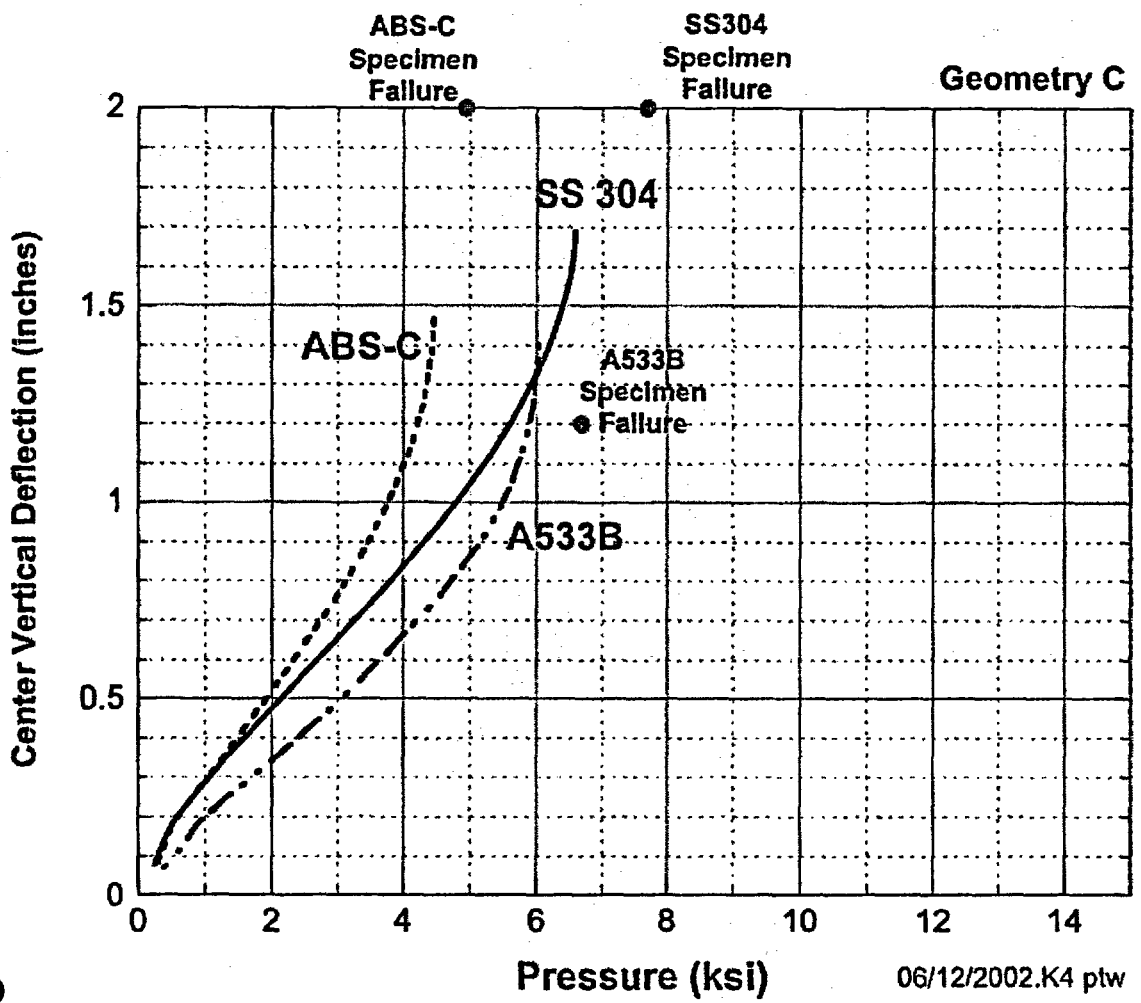

(d)

Fig. 5. (continued) (d) ABAQUS FEM vertical deflection histories at the center of Geometry C, all three materials compared to specimen failure.

Table 4. Comparison of Experimental Burst Pressures to Three Predictions

Test Number	Material	Geometry	Experimental		Riccardella's ASME Paper			Hill's Plastic Instability Theory			ABAQUS Solutions		
			Burst Pressure (BP) (ksi)	Location of Failure	Predicted Burst Pressure (BP) (ksi)	Location of Failure	Exp. BP/ Predicted BP	Predicted Burst Pressure (BP) (ksi)	Location of Failure	Exp. BP/ Predicted BP	Predicted Burst Pressure (BP) (ksi)	Location of Failure	Exp. BP/ Predicted BP
1	SS 304	A	15	Edge	12.3	Edge	1.22	12.98	Center	1.16	13.29	Edge	1.13
2		B	6.8	Center	4.8	Edge	1.42	5.92	Center	1.15	6.22	Edge	1.09
3		C	7.7	Center	7.4	Center	1.04	6.49	Center	1.19	6.59	Center	1.17
4	A533B	A	11	Edge	9.8	Edge	1.12	12.37	Center	0.89	12.26	Edge	0.90
5		B	5.3	Edge	4.2	Edge	1.26	5.65	Center	0.94	5.24	Edge	1.01
6		C	6.7	Center	6.8	Center	0.99	6.19	Center	1.08	6.03	Edge	1.11
7	ABS-C	A	9.8	Edge	8	Edge	1.23	8.95	Center	1.10	9.05	Edge	1.08
8		B	3.75	Edge	3	Edge	1.25	4.08	Center	0.92	4.19	Edge	0.89
9		C	4.94	Edge				4.47	Center	1.10	4.46	Edge/Center	1.11

3.2. Development of Stochastic Model of Failure

The development of several stochastic models is described in this section in which the uncertainties associated with predictions of burst pressure for circular diaphragms using computational or analytical methods are estimated. It is postulated that the trends observed in estimating the burst pressure with the nine disk-burst tests in [2] will be representative of the predictive accuracy of computational estimates of the burst pressure in the Davis-Besse wastage-area problem. Given a prediction of burst pressure for a specific configuration of the wastage area, the scaled stochastic models will provide estimates of the cumulative probability that the true burst pressure will be less than a given service pressure. This postulated linkage of the test specimens to the Davis-Besse problem is obviously an approximation, since the wastage area footprints are not identical to the circular diaphragms used in the tests. The appropriateness of this linkage is in part, therefore, dependent on the ability of the finite-element models to capture, as accurately as is feasible and based on the best current knowledge, the actual geometry of the wastage area footprint.

Table 5 summarizes some descriptive statistics for the ratio of experimental burst pressure to predicted burst pressure, α, for the three predictive methods discussed in the previous section. Also shown in the table are the results of combining the three samples into one larger sample of 26 data points. This combined sample was used to develop the stochastic models with α treated as a random variate. Combining the three sets into a single sample produced a sample size large enough to make a thorough statistical analysis of a range of continuous distributions feasible. Also given in Table 6 is a ranking of the 26 data points where the median rank order statistic is

$$P_{(i)} = \frac{i-0.3}{n+0.4} \tag{16}$$

The *Expert Fit*© [9] computer program was used to develop several stochastic models of the sample data presented in Table 6. Using a combination of heuristic criteria and *Goodness of Fit* statistics, twenty six continuous distributions were tested with the results shown in ranked order in Table 7. The point-estimation procedures noted in Table 7 include *Maximum Likelihood* (*ML*), *Method of Moments* (*MM*), and *Quantile Estimates*. Table 8 compares three *Goodness of Fit* statistics (Anderson-Darling, χ^2, and Kolmogorov-Smirnoff (*K-S*)) for the top six distributions. None of these distributions were rejected by the *Goodness of Fit* tests, and all received an absolute rating of *Good* by the *Expert Fit*© computer program. The remaining nineteen distributions investigated were either rejected by one or more of the *Goodness of Fit* tests at some significance level and/or received a less than *Good* heuristic rating by the *Expert Fit*© software. Figure 6 shows a density/histogram overplot of the six continuous distributions.

Table 5. Descriptive Statistics for the Ratio of Experimental Burst Pressure to Predicted Burst Pressures

Descriptive Statistics	Riccardella (1972)	Hill's Theory	ABAQUS	Combined
Sample Size	8	9	9	26
Mean	1.1902	1.0576	1.0549	1.0975
Standard Error	0.0484	0.0374	0.0331	0.0251
Median	1.2223	1.0953	1.0939	1.1057
Standard Deviation	0.1368	0.1123	0.0993	0.1281
Sample Variance	0.0187	0.0126	0.0099	0.0164
Kurtosis	-0.0506	-1.4799	-0.4349	0.2593
Skewness	0.0007	-0.5892	-0.9683	0.1714
Range	0.4314	0.2979	0.2739	0.5277
Minimum	0.9853	0.8889	0.8943	0.8889
Maximum	1.4167	1.1868	1.1682	1.4167
Confidence Level(95.0%)	0.1144	0.0863	0.0764	0.0517

Table 6. Combined Sample Used in Development of Stochastic Model

Rank	Method	Material	Geometry	α^*	Order Statistic
1	Hill's Theory	A533B	A	0.8889	0.0265
2	ABAQUS Soln.	ABS-C	B	0.8943	0.0644
3	ABAQUS Soln.	A533B	A	0.8972	0.1023
4	Hill's Theory	ABS-C	B	0.9180	0.1402
5	Hill's Theory	A533B	B	0.9382	0.1780
6	Ricarrdella (1972)	A533B	C	0.9853	0.2159
7	ABAQUS Soln.	A533B	B	1.0119	0.2538
8	Ricarrdella (1972)	SS 304	C	1.0405	0.2917
9	ABAQUS Soln.	ABS-C	A	1.0827	0.3295
10	Hill's Theory	A533B	C	1.0829	0.3674
11	ABAQUS Soln.	SS 304	B	1.0939	0.4053
12	Hill's Theory	ABS-C	A	1.0953	0.4432
13	Hill's Theory	ABS-C	C	1.1042	0.4811
14	ABAQUS Soln.	ABS-C	C	1.1072	0.5189
15	ABAQUS Soln.	A533B	C	1.1104	0.5568
16	Ricarrdella (1972)	A533B	A	1.1224	0.5947
17	ABAQUS Soln.	SS 304	A	1.1288	0.6326
18	Hill's Theory	SS 304	B	1.1479	0.6705
19	Hill's Theory	SS 304	A	1.1560	0.7083
20	ABAQUS Soln.	SS 304	C	1.1682	0.7462
21	Hill's Theory	SS 304	C	1.1868	0.7841
22	Ricarrdella (1972)	SS 304	A	1.2195	0.8220
23	Ricarrdella (1972)	ABS-C	A	1.2250	0.8598
24	Ricarrdella (1972)	ABS-C	B	1.2500	0.8977
25	Ricarrdella (1972)	A533B	B	1.2619	0.9356
26	Ricarrdella (1972)	SS 304	B	1.4167	0.9735

$^*\alpha$ = Experimental Burst Pressure/Predicted Burst Pressure

Table 7. Continuous Distributions Investigated – Ranked by Goodness of Fit

Model	Parameters	Point Estimator	Parameter Values
1 - Log-Laplace	Location	Default	0
	Scale	ML estimate	1.1057
	Shape	ML estimate	11.45441
2 - Beta	Lower endpoint	MOM estimate	0.61449
	Upper endpoint	MOM estimate	1.78866
	Shape #1	MOM estimate	7.95564
	Shape #2	MOM estimate	11.38552
3 - Gamma	Location	Default	0
	Scale	ML estimate	0.01444
	Shape	ML estimate	76.01293
4 - Log-Logistic	Location	Default	0
	Scale	ML estimate	1.09586
	Shape	ML estimate	15.21867
5 - Normal	Mean	ML estimate	1.09747
	Standard Dev.	ML estimate	0.12811
6 - Weibull	Location	Default	0
	Scale	ML estimate	1.15383
	Shape	ML estimate	9.03948
7 - Lognormal	Location	Default	0
	Scale	ML estimate	0.08641
	Shape	ML estimate	0.11516
8 - Random Walk	Location	Default	0
	Scale	ML estimate	0.92335
	Shape	ML estimate	69.18788
9 - Inverse Gaussian	Location	Default	0
	Scale	ML estimate	1.09747
	Shape	ML estimate	82.23451
10 - Pearson Type V	Location	Default	0
	Scale	ML estimate	81.42582
	Shape	ML estimate	75.1846
11 - Inverted Weibull	Location	Default	0
	Scale	ML estimate	1.02827
	Shape	ML estimate	8.88835
12 - Weibull(E)	Location	Quantile estimate	0.88884
	Scale	ML estimate	0.21562
	Shape	ML estimate	1.15868
13 - Rayleigh(E)	Location	Quantile estimate	0.88884
	Scale	ML estimate	0.24352
14 - Erlang(E)	Location	Quantile estimate	0.88884
	Scale	ML estimate	0.20862
	Shape	ML estimate	1
15 - Gamma(E)	Location	Quantile estimate	0.88884
	Scale	ML estimate	0.21819
	Shape	ML estimate	0.95616
16 - Exponential(E)	Location	ML estimate	0.8889
	Scale	ML estimate	0.20857
17 - Pearson Type VI(E)	Location	Quantile estimate	0.88884
	Scale	Default	1
	Shape #1	ML estimate	1.00117

Model	Parameters	Point Estimator	Parameter Values
	Shape #2	ML estimate	5.43892
18 - Lognormal(E)	Location	Quantile estimate	0.88884
	Scale	ML estimate	-2.17414
	Shape	ML estimate	1.86865
19 - Random Walk(E)	Location	Quantile estimate	0.88884
	Scale	ML estimate	699.32509
	Shape	ML estimate	4.82644
20 - Pareto(E)	Location	ML estimate	0.8889
	Shape	ML estimate	4.8976
21 - Chi-Square	Location	Quantile estimate	0.88884
	d.f.	ML estimate	0.72313
22 - Wald	Location	Default	0
	Shape	ML estimate	48.03951
23 - Rayleigh	Location	Default	0
	Scale	ML estimate	1.10463
24 - Exponential	Location	Default	0
	Scale	ML estimate	1.09747
25 - Wald(E)	Location	Quantile estimate	0.88884
	Shape	ML estimate	1.43E-03
26 - Inverse Gaussian(E)	Location	Quantile estimate	8.89E-04
	Scale	ML estimate	0.20862
	Shape	ML estimate	1.44E-03

Table 8. Continuous Distributions That Passed All Goodness of Fit Tests

Rank	Model	Relative Score	Rating	Anderson-Darling	χ2 Statistic	K-S
1	Log-Laplace	98	Good	0.44952	2.15385	0.59218
2	Beta	93	Good	0.44697	4.92308	0.81037
3	Gamma	89	Good	0.46050	3.53846	0.81894
4	Normal	83	Good	0.39325	1.23077	0.74664
5	Random Walk	75	Good	0.50448	3.53846	0.85840
6	Inverse Gaussian	71	Good	0.50514	3.53846	0.85891

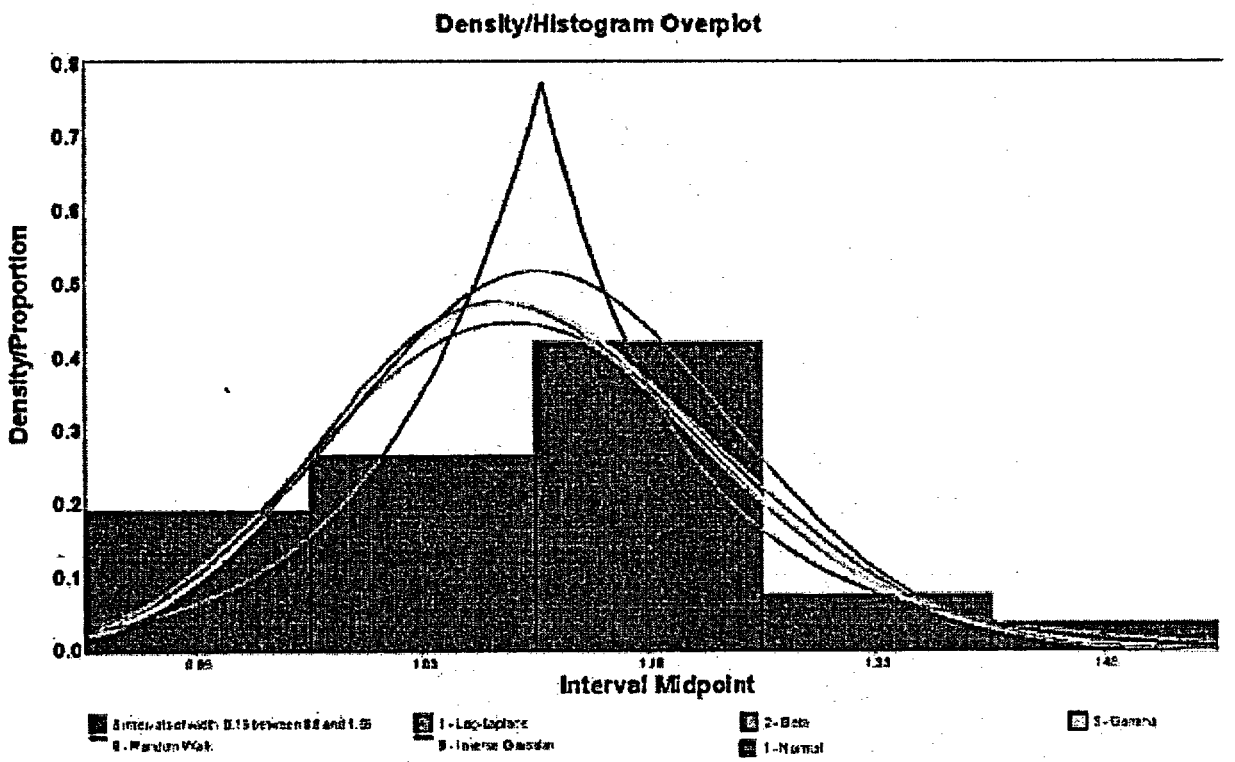

Fig. 6. Overplot of probability densities with histogram for fitted stochastic models.

The six distributions in Table 8 have the following analytical forms:

Log-Laplace Distribution

The Log-Laplace distribution has the highest relative ranking among the twenty-six distributions investigated. The general three-parameter Log-Laplace continuous distribution has the following probability density function, f_{LP}, and cumulative distribution function, F_{LP},

$$f_{LP}(x|\,a,b,c)=\begin{cases}\dfrac{c}{2b}\left(\dfrac{x-a}{b}\right)^{c-1} & \text{for } a<x<b\\ \dfrac{c}{2b}\left(\dfrac{x-a}{b}\right)^{-c-1} & \text{for } x\geq b\end{cases} \qquad \text{for } a\geq 0,\ (b,c)>0$$

$$\Pr(X\leq x)=F_{LP}(x|\,a,b,c)=\begin{cases}\dfrac{1}{2}\left(\dfrac{x-a}{b}\right)^{c} & \text{for } a<x<b\\ 1-\dfrac{1}{2}\left(\dfrac{x-a}{b}\right)^{-c} & \text{for } x\geq b\end{cases} \qquad \text{for } a\geq 0,\ (b,c)>0 \tag{17}$$

where a is the location parameter, b is the scale parameter, and c is the shape parameter.

Beta Distribution

The Beta distribution has the following probability density function, f_{Be}, and cumulative distribution function, F_{Be},

$$f_{Be}(x|\,a,b,\alpha_1,\alpha_2)=\begin{cases}\dfrac{\left(\dfrac{x-a}{b-a}\right)^{\alpha_1-1}\left[1-\left(\dfrac{x-a}{b-a}\right)\right]^{\alpha_2-1}}{(b-a)B(\alpha_1,\alpha_2)} & \text{for } a<x<b\\ 0 & \text{otherwise}\end{cases}$$

$$F_{Be}(x|\,a,b,\alpha_1,\alpha_2)=\begin{cases}\displaystyle\int_a^x f_{Be}(\xi|\,a,b,\alpha_1,\alpha_2)\,d\xi & \text{for } a<x<b\\ 0 & \text{otherwise}\end{cases} \tag{18}$$

where $B(\alpha_1,\alpha_2)=\displaystyle\int_0^1 u^{\alpha_1-1}(1-u)^{\alpha_2-1}du$, a is the lower endpoint, b is the upper endpoint, α_1 is the first shape parameter, and α_2 is the second shape parameter.

Gamma Distribution

The Gamma distribution has the following probability density function, f_{Ga}, and cumulative distribution function, F_{Ga},

$$f_{Ga}(x|\alpha,\beta,\gamma)=\begin{cases}\dfrac{(x-\gamma)^{\alpha-1}}{\beta^{\alpha}\Gamma(\alpha)}\exp\left[-\left(\dfrac{x-\gamma}{\beta}\right)\right] & \text{for } x>\gamma\\ 0 & \text{otherwise}\end{cases}$$

$$F_{Ga}(x|\alpha,\beta,\gamma)=\begin{cases}\displaystyle\int_{\gamma}^{x} f_{Ga}(\xi|\alpha,\beta,\gamma)\,d\xi & \text{for } x>\gamma\\ 0 & \text{otherwise}\end{cases} \qquad (19)$$

where α is the shape parameter, β is the scale parameter, γ is the location parameter, and $\Gamma(x)=\int_0^{\infty}\exp(-u)u^{x-1}du$.

Normal Distribution

The Normal distribution has the following probability density function, f_N, and cumulative distribution function, F_N,

$$f_N(x|\mu,\sigma)=\frac{1}{\sqrt{2\pi\sigma^2}}\exp\left[\frac{-(x-\mu)^2}{2\sigma^2}\right] \text{ for all real numbers } x$$

$$F_N(x|\mu,\sigma)=\Phi(z)=\int_{-\infty}^{z} f_N(\xi|0,1)d\xi \text{ for } z=(x-\mu)/\sigma \qquad (20)$$

where μ is the mean (location parameter) and σ is the standard deviation (scale parameter).

Random Walk Distribution

The Random Walk distribution has the following probability density function, f_{RW}, and cumulative distribution function, F_{RW}

$$f_{RW}(x|\alpha,\beta,\gamma)=\begin{cases}\left(\dfrac{\alpha}{2\pi(x-\gamma)}\right)^{1/2}\exp\left\{\dfrac{-\alpha\left[1-\beta(x-\gamma)\right]^2}{2\beta^2(x-\gamma)}\right\} & \text{for } x>\gamma\\ 0 & \text{otherwise}\end{cases}$$

$$F_{RW}(x|\alpha,\beta,\gamma)=\begin{cases}\Phi\left\{-\left[\dfrac{1}{\beta(x-\gamma)}-1\right]\sqrt{\alpha(x-\gamma)}\right\}- \\ \quad \exp\left(\dfrac{2\alpha}{\beta}\right)\Phi\left\{-\left[\dfrac{1}{\beta(x-\gamma)}+1\right]\sqrt{\alpha(x-\gamma)}\right\} & \text{for } x>\gamma\\ 0 & \text{otherwise}\end{cases} \quad (21)$$

where α is the shape parameter, β is the scale parameter, γ is the location parameter, and Φ is defined in Eq. (20).

Inverse Gaussian (Wald) Distribution

The Inverse Gaussian (also known as the Wald distribution) distribution has the following probability density function, f_{IG}, and cumulative distribution function, F_{IG}

$$f_{IG}(x|\alpha,\beta,\gamma)=\begin{cases}\left[\dfrac{\alpha}{2\pi(x-\gamma)^3}\right]^{1/2}\exp\left[\dfrac{-\alpha(x-\gamma-\beta)^2}{2\beta^2(x-\gamma)}\right] & \text{for } x>\gamma\\ 0 & \text{otherwise}\end{cases}$$

$$F_{IG}(x|\alpha,\beta,\gamma)=\begin{cases}\Phi\left[\left(\dfrac{x-\gamma}{\beta}-1\right)\sqrt{\dfrac{\alpha}{x-\gamma}}\right]+\exp\left[\dfrac{2\alpha}{\beta}\right]\Phi\left[-\left(\dfrac{x-\gamma}{\beta}+1\right)\sqrt{\dfrac{\alpha}{x-\gamma}}\right] & \text{for } x>\gamma\\ 0 & \text{otherwise}\end{cases} \quad (22)$$

where α is the shape parameter, β is the scale parameter, γ is the location parameter, and Φ is defined in Eq. (20).

Figures 7 and 8 compare the probabilities and the cumulative distribution functions, respectively, of the top-three ranked models.

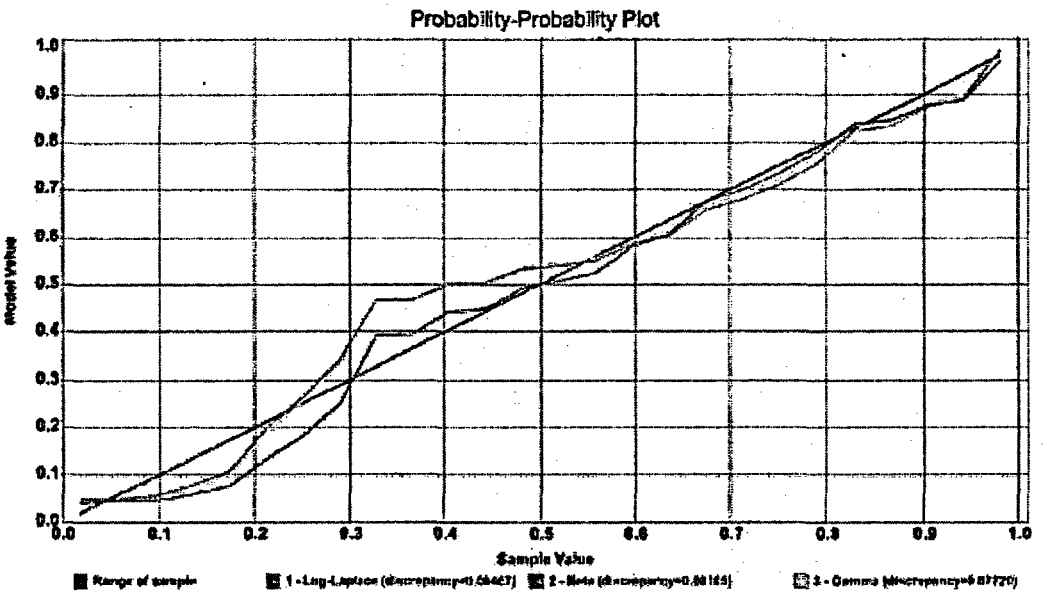

Fig. 7. Probability-probability plot comparing top three fitted distributions.

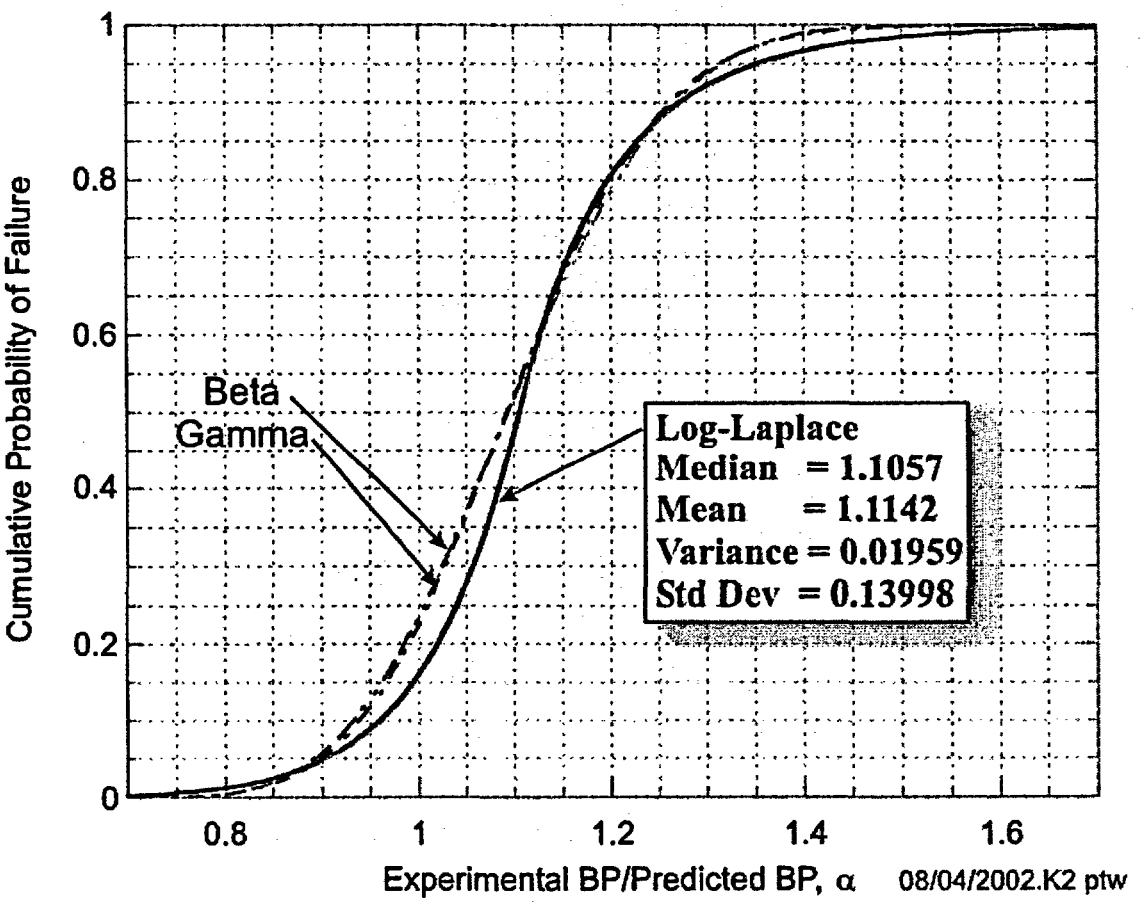

Fig. 8. Log-Laplace statistical failure model ($n = 26$) compared to a beta and gamma cumulative distribution functions.

As a specific example from the *Expert Fit*© [9] analysis, the Log-Laplace stochastic model of failure has the following form

$$f_{LP}(\alpha|0,1.1057,11.45441)=\begin{cases}5.17971\left(\dfrac{\alpha}{1.1057}\right)^{10.45441} & ;\ 0<\alpha<1.1057\\ 5.17971\left(\dfrac{\alpha}{1.1057}\right)^{-12.45441} & ;\ \alpha\geq 1.1057\end{cases}$$

$$\Pr(X\leq\alpha)=F_{LP}(\alpha|0,1.1057,11.45441)=\begin{cases}\dfrac{1}{2}\left(\dfrac{\alpha}{1.1057}\right)^{11.45441} & ;\ 0<\alpha<1.1057\\ 1-\dfrac{1}{2}\left(\dfrac{\alpha}{1.1057}\right)^{-11.45441} & ;\ \alpha\geq 1.1057\end{cases} \quad (23)$$

where α is the ratio of the true (but unknown) burst pressure to the calculated burst pressure. The percentile function is given by

$$Q_{LP}(P|0,1.1057,11.45441)=\alpha=\begin{cases}1.1057\exp\left\{\dfrac{\ln(2P)}{11.45441}\right\} & ;\ P\leq 0.5\\ 1.1057\exp\left\{\dfrac{-\ln[2(1-P)]}{11.45441}\right\} & ;\ P>0.5\end{cases} \quad \text{for } (0<P<1) \quad (24)$$

The stochastic models in Table 8 can be used to provide statistical estimates of the expected predictive accuracy of computational methods applied to burst pressure calculations for service pressures within the range of the data used to develop the model, i.e., $0.8889\times P_{BP}\leq SP\leq 1.4167\times P_{BP}$, where, SP, is a service pressure, and P_{BP} is the predicted burst pressure for the condition under investigation. Extrapolating significantly beyond the range of the data becomes somewhat problematic due to the small sample size of twenty-six data points. All six models in Table 8 are plausible candidates to describe the population from which the sample in Table 6 was drawn, and the relative ranking of these distributions may be sensitive to sample size.

Table 9 provides an example of the sensitivity of the fitting process to the sample size for the case of the "as-found" cavity condition (to be discussed in the next section). Normal distributions were fitted to two samples from the predictions of the disk-burst tests: (1) the ABAQUS finite-element results (n = 9) and (2) the combined data set (n = 26). The two stochastic models were then scaled by the failure pressure for the "as-found" condition (failure pressure = 6.65 ksi). Extrapolating beyond the range of the data for the "as-found" case study produces approximately three orders-of-magnitude difference in estimated failure probability at the operating pressure of 2.165 ksi. This difference in estimated failure probability decreases as the service pressure increases towards the range of data used to develop the models.

Table 9. Sensitivity of Cumulative Probability of Failure to Sample Size: "As-Found" Condition (see Sect. 4)

Internal Pressure (ksi)	Normal Distribution	
	ABAQUS n=9	Combined n=26
6.65	0.2902	0.2233
2.155	1.04E-12	7.81E-10
2.165	1.17E-12	8.40E-10
2.200	1.53E-13	1.08E-09
2.225	2.02E-13	1.30E-09
2.250	2.68E-13	1.55E-09
2.275	3.53E-13	1.85E-09
2.300	4.66E-13	2.21E-09
2.325	6.13E-13	2.64E-09
2.350	8.05E-13	3.14E-09
2.375	1.06E-12	3.75E-09
2.400	1.39E-12	4.46E-09
2.425	1.81E-12	5.30E-09
2.450	2.37E-12	6.30E-09
2.475	3.09E-12	7.48E-09
2.500	4.03E-12	8.87E-09

4. Application of Stochastic Model to Bounding Calculation

A bounding calculation was carried out for the "as-found" condition of the wastage area in the Davis-Besse head. The finite-element model used in the analysis is shown in Fig. 9. An adjusted stress-strain curve (see Fig. 10) was constructed to lower-bound the available data for the cladding material. The geometry of the wastage area footprint was taken from Fig. 13 in the *Root Cause Analysis Report* [10]. As an estimate of the uncertainty in the current wastage area measurements, the footprint was extended by approximately 0.25 inches (see Table 10 and Fig. 11 for a geometric description of the adjusted footprint). A uniform cladding thickness of 0.24 inches (the minimum cladding thickness value shown in Fig. 14 of ref. [10]) was assumed in the model. The finite-element model was then loaded with increasing pressure until the point of numerical instability at an internal pressure of 6.65 ksi (see Fig. 12). In the following, an example is provided of how the statistical distributions in Table 8 can be scaled and applied to the analysis of failure of the cladding in the wastage area.

For the predicted burst pressure of 6.65 ksi, the Log-Laplace statistical failure model as an example can be scaled to provide estimates of cumulative probability of failure (or probability of nonexceedance) as a function of internal service pressure for the specific condition of the wastage area simulated by the finite-element analysis. The scaled Log-Laplace model (see Fig. 13) has the following form

$$f_{LP}(SP\,|P_{BP}) = \begin{cases} 5.17971\left(\dfrac{SP}{1.1057\times P_{BP}}\right)^{10.45441} & ;\ 0<SP<1.1057\times P_{BP} \\ 5.17971\left(\dfrac{SP}{1.1057\times P_{BP}}\right)^{-12.45441} & ;\ SP\geq 1.1057\times P_{BP} \end{cases}$$

$$\Pr(P_{BP(true)}\leq SP) = F_{LP}(SP\,|\,P_{BP}) = \begin{cases} \dfrac{1}{2}\left(\dfrac{SP}{1.1057\times P_{BP}}\right)^{11.45441} & ;\ 0<SP<1.1057\times P_{BP} \\ 1-\dfrac{1}{2}\left(\dfrac{SP}{1.1057\times P_{BP}}\right)^{-11.45441} & ;\ SP\geq 1.1057\times P_{BP} \end{cases} \quad (25)$$

where, SP, is the service pressure under consideration, P_{BP} is the predicted burst, and $P_{PB(true)}$ is the unknown true burst pressure. The scaled percentile function is

$$Q_{LP}(P\,|0,1.1057\times P_{BP},11.45441) = SP = \begin{cases} 1.1057\times P_{BP}\exp\left\{\dfrac{\ln(2P)}{11.45441}\right\} & ;\ P\leq 0.5 \\ 1.1057\times P_{BP}\exp\left\{\dfrac{-\ln[2(1-P)]}{11.45441}\right\} & ;\ P>0.5 \end{cases} \quad \text{for } (0<P<1) \quad (26)$$

Table 10. Wastage-Area-Footprint Geometry Data

Description	Scaling Factor	Area	Perimeter	Centroid of Wastage Area Footprint		Moments of Inertia About the Centroid			Eigenvalue Extraction for Principal Moments and Directions			
									Principal Moments		Principal Directions	
		(in^2)	(in.)	x_c (in.)	y_c (in.)	I_{xx} (in^4)	I_{yy} (in^4)	I_{xy} (in^4)	I_1 (in^4)	I_2 (in^4)	I_1	I_2
As-Found Footprint	1	35.36	30.36	16.4122	-0.1194	98.89	9699.33	-117.16	75.26	197.41	<0.9004, -0.4351>	<0.4351, 0.9004>
Adjusted Footprint for Bounding Calculation	0.25 in.	40.06	31.78	16.4301	-0.1255	129.02	11031.81	-141.35	99.00	245.71	<0.8943, -0.4476>	<0.4476, 0.8943>

Footprint centroid is in global coordinates.
Global coordinate system has its z-axis aligned with the vertical centerline of the vessel.
The x-y plane of the global coordinate system is a horizontal plane
with the x-axis along the line between the centerlines of Nozzles 3 and 11.

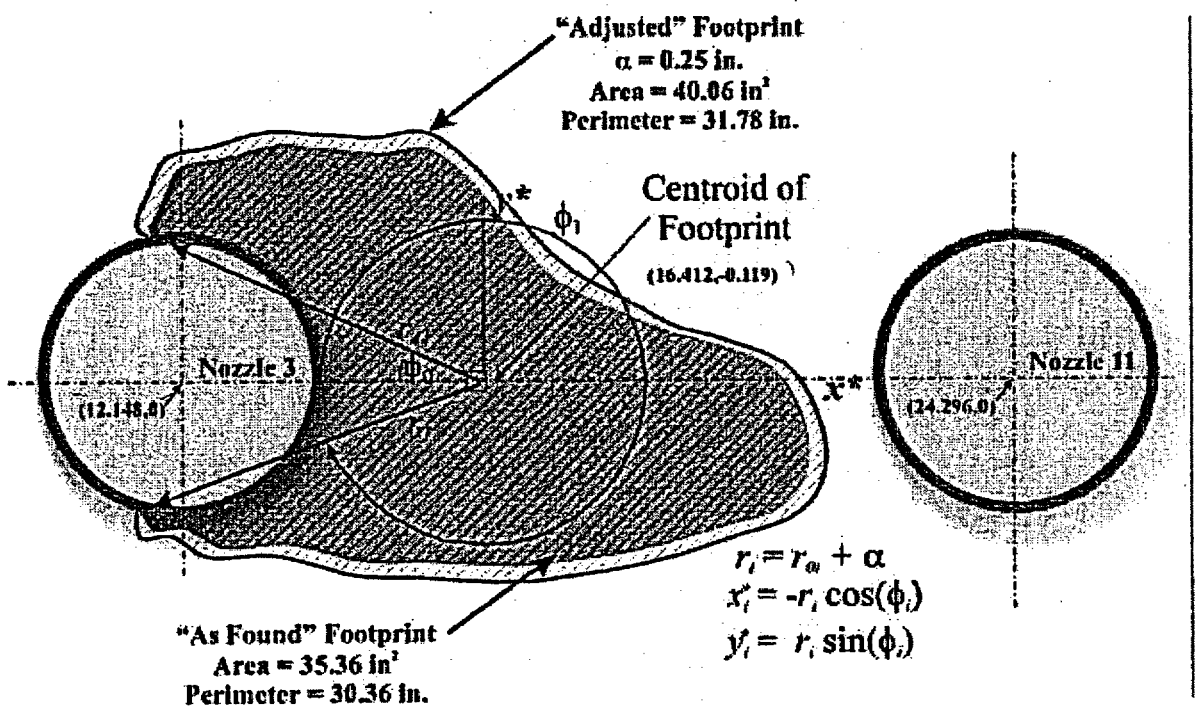

Table 10 (continued) Details of Wastage Area Footprint Before Adjustment for Bounding Calculation (Figure taken from Fig. 13 ref. [10])

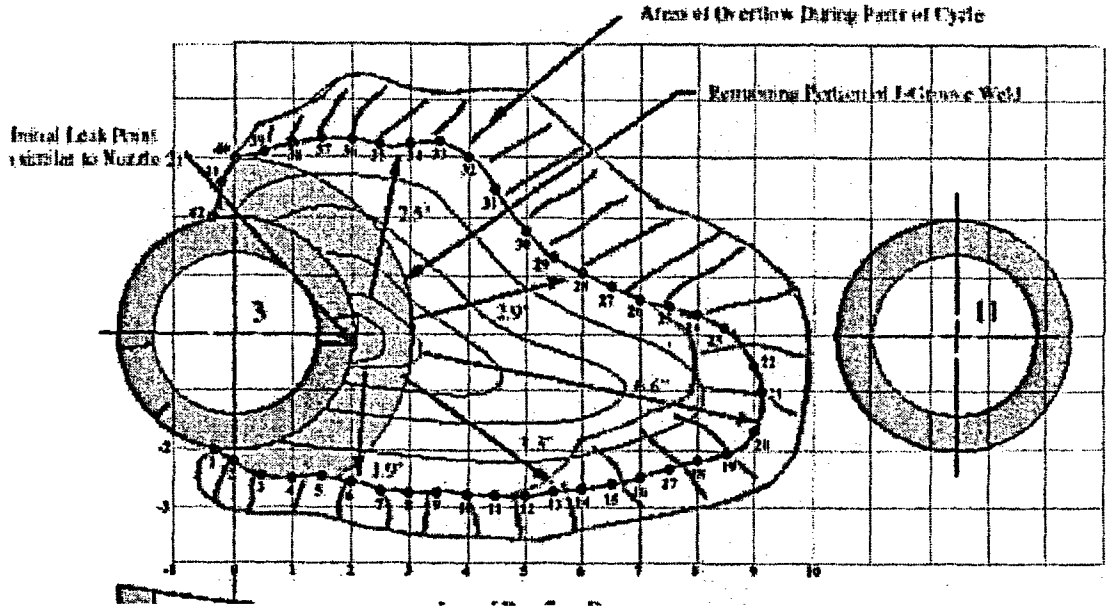

Point	x*	y*	Point	x*	y*
0	-0.639	-1.895	24	8.000	0.334
1	-0.334	-2.280	25	7.500	0.483
2	0.000	-2.235	26	7.000	0.582
3	0.500	-2.492	27	6.500	0.829
4	1.000	-2.522	28	6.000	1.046
5	1.500	-2.482	29	5.500	1.303
6	2.000	-2.581	30	5.000	1.778
7	2.500	-2.730	31	4.500	2.460
8	3.000	-2.769	32	4.000	3.023
9	3.500	-2.759	33	3.500	3.300
10	4.000	-2.789	34	3.000	3.221
11	4.500	-2.819	35	2.500	3.250
12	5.000	-2.819	36	2.000	3.300
13	5.500	-2.759	37	1.500	3.349
14	6.000	-2.700	38	1.000	3.240
15	6.500	-2.621	39	0.500	3.122
16	7.000	-2.512	40	0.000	3.000
17	7.500	-2.364	41	-0.210	2.578
18	8.000	-2.216	42	-0.364	2.000
19	8.500	-2.087	43	-0.242	1.985
20	9.000	-1.712			
21	9.135	-1.000			
22	9.000	-0.555			
23	8.500	0.137			

Origin of local coordinate system located at centerline of Nozzle 3. (inches)

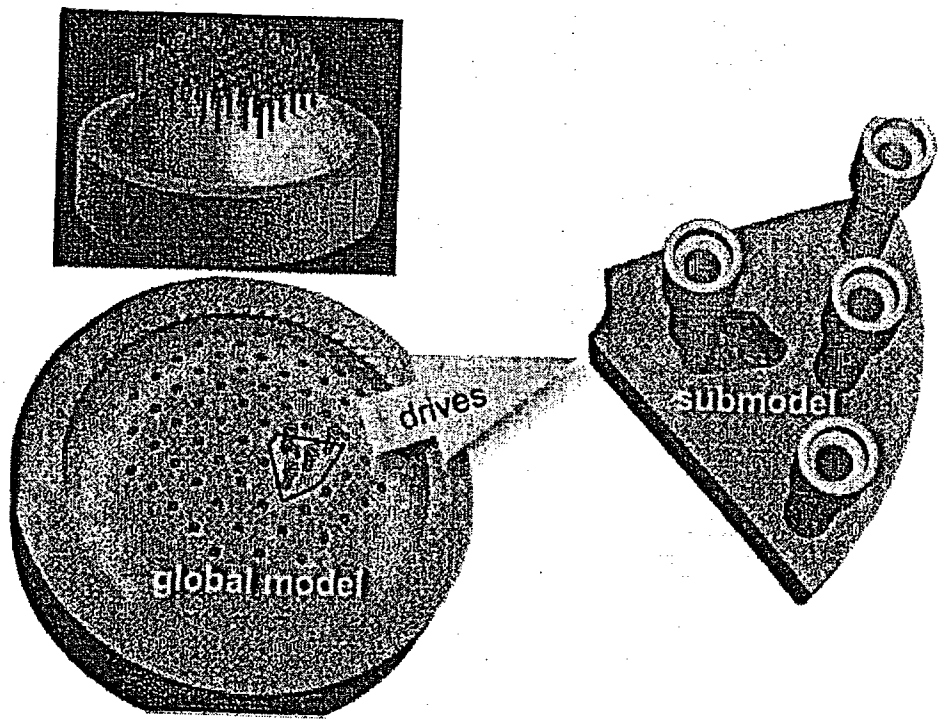

(a)

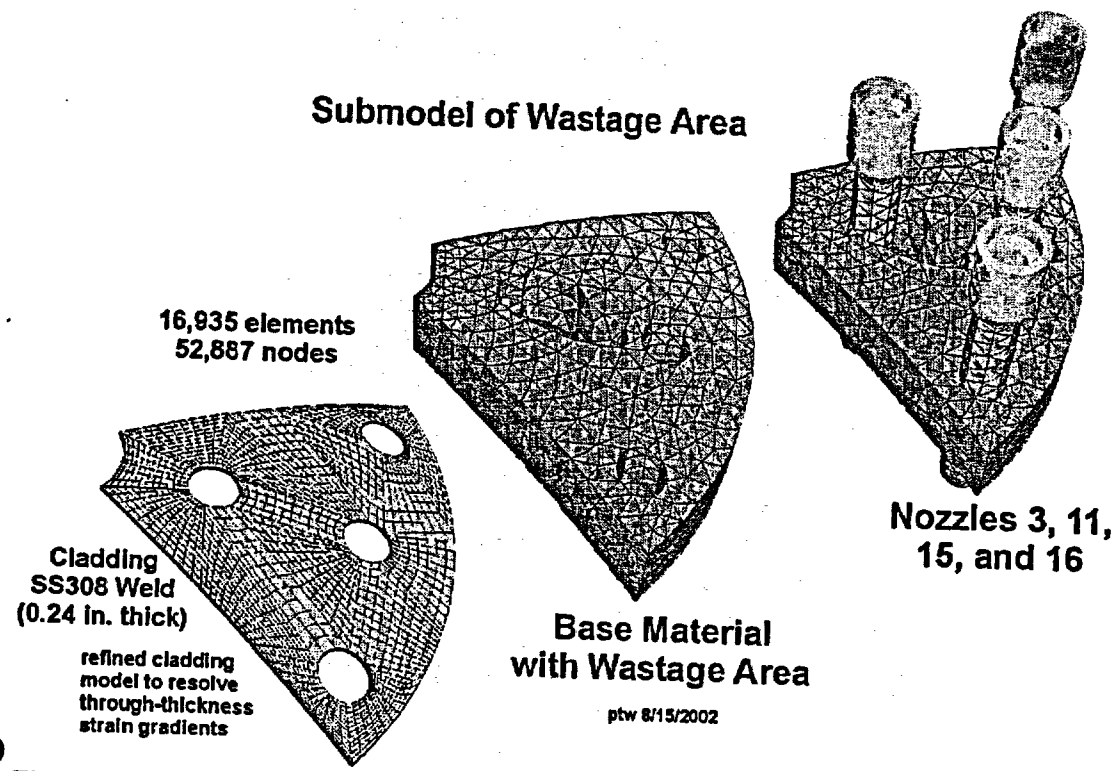

(b)

Fig. 9. Finite-element global and submodels of the Davis-Besse head and wastage area. The displacements at the vertical side boundaries of the submodel are driven by the global model. Both models are exposed to the same internal pressure loading.

(c)

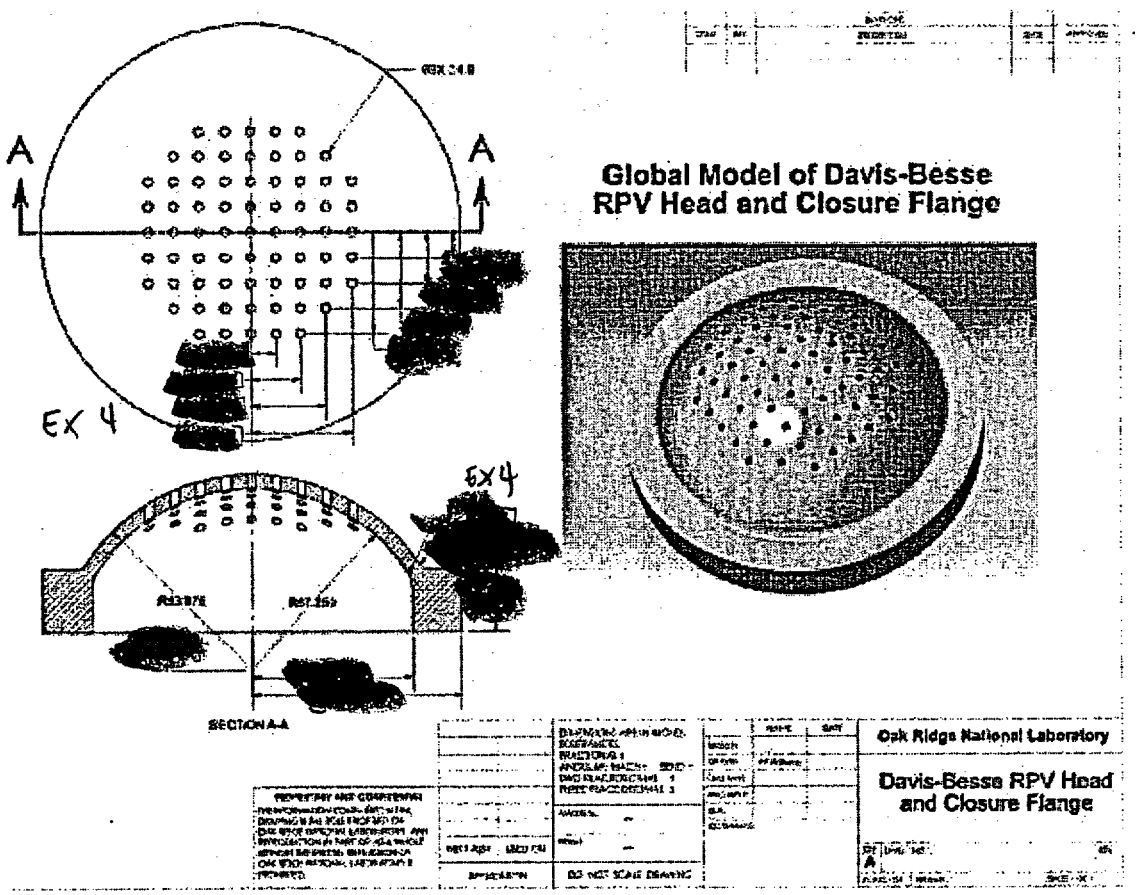

Fig 9. (continued) (c) geometry of RPV head and closure flange used in global model,

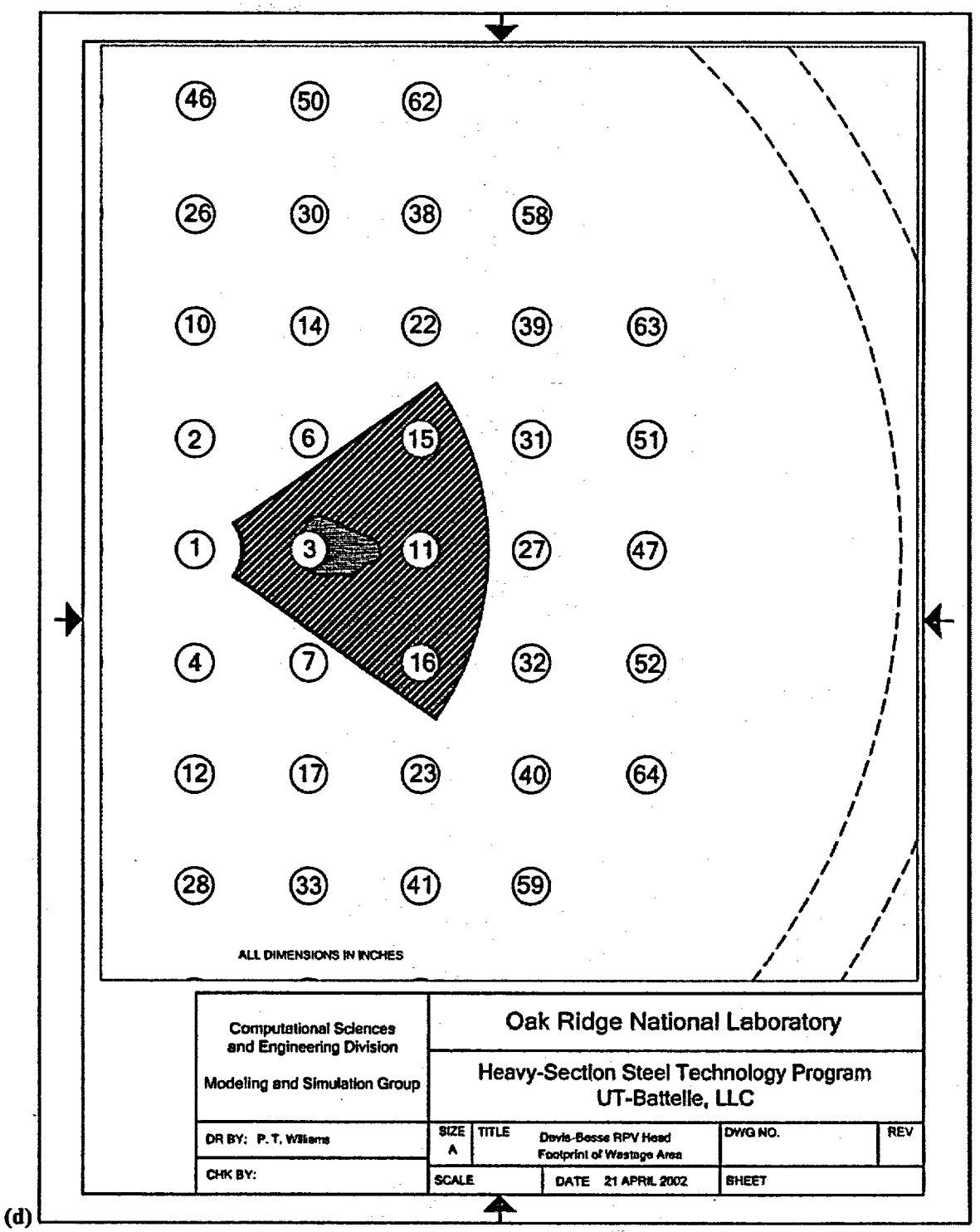

(d)

Fig 9. (continued) (d) relative location of submodel within full RPV head,

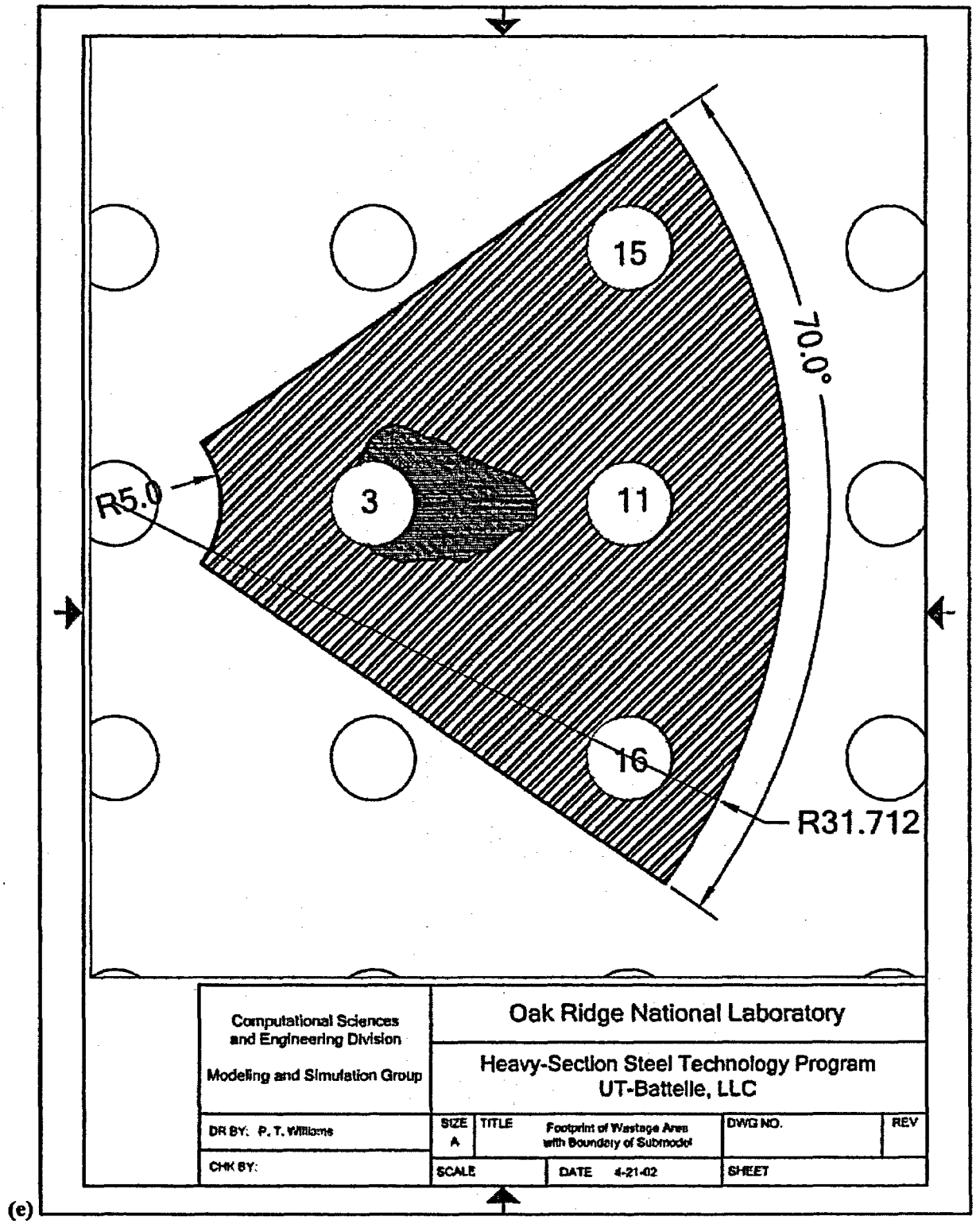

(e)

Fig 9. (continued) (e) geometry of submodel relative to Nozzles 3, 11, 15, and 16.

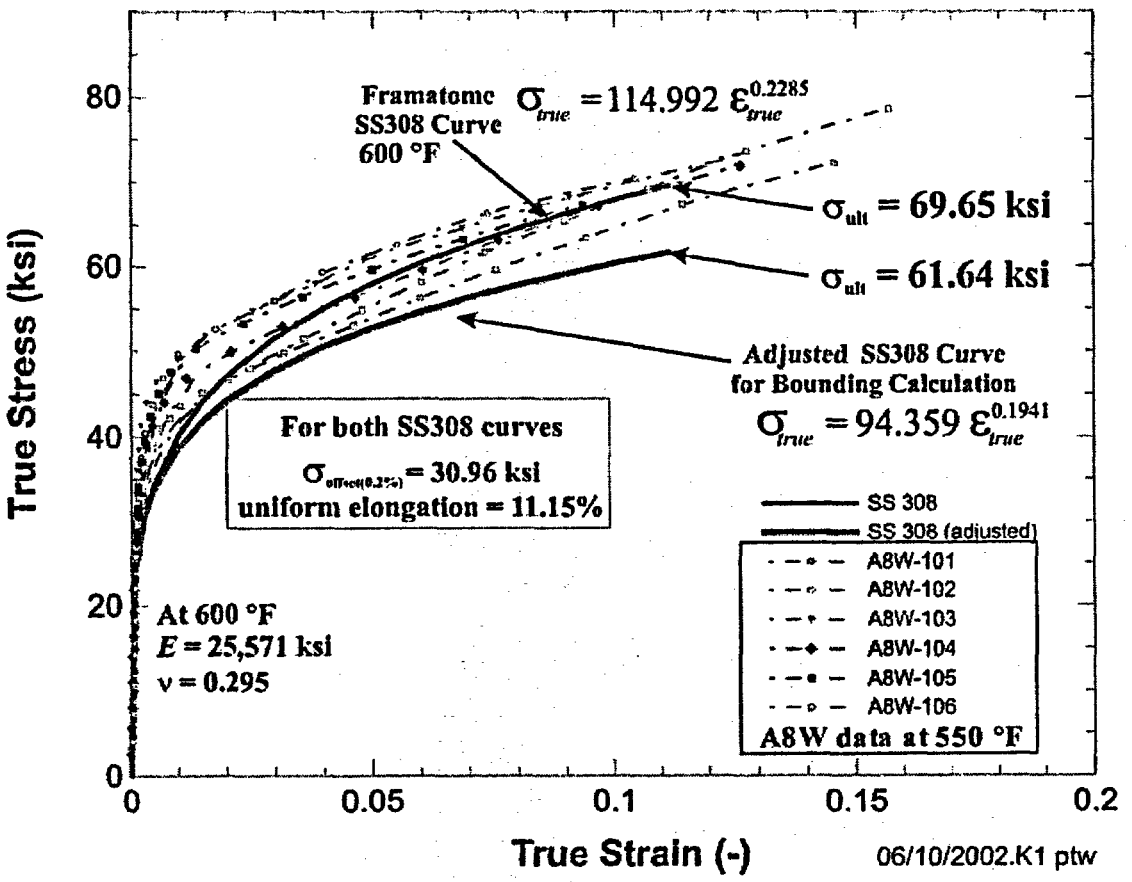

Fig. 10. Adjusted SS308 stress vs. strain curve used in the bounding-case calculations compared to curves from a range of A8W heats. Strain hardening in the adjusted curve was reduced to lower-bound all of the data. The offset yield strength and strain at ultimate strength were retained from the unadjusted SS308 curve received from Framatome.

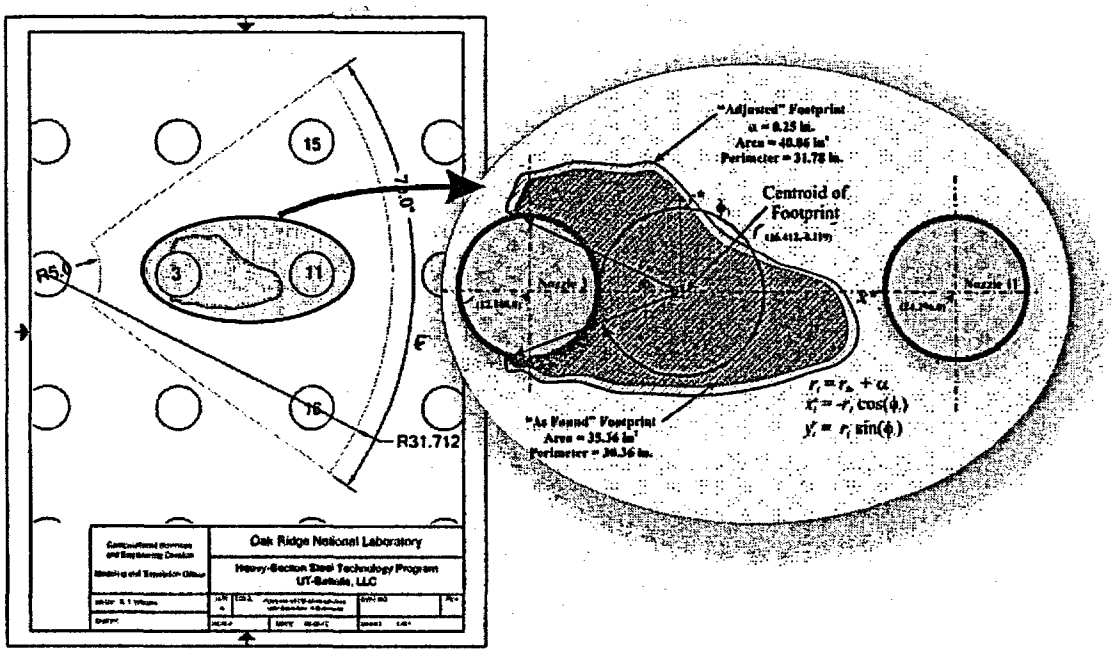

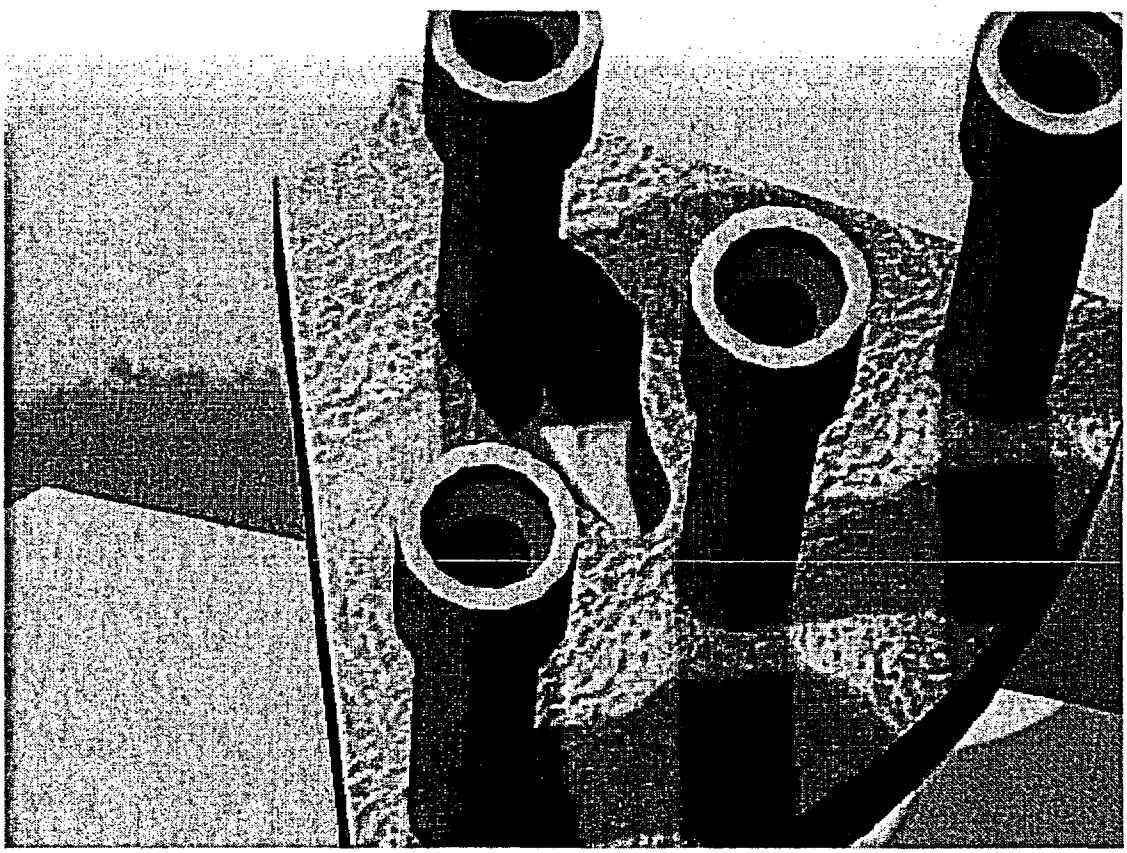

Fig. 11. Geometry of adjusted wastage area footprint. Lower figure is a Photoworks®-rendered image of the submodel with the adjusted "as-found" footprint.

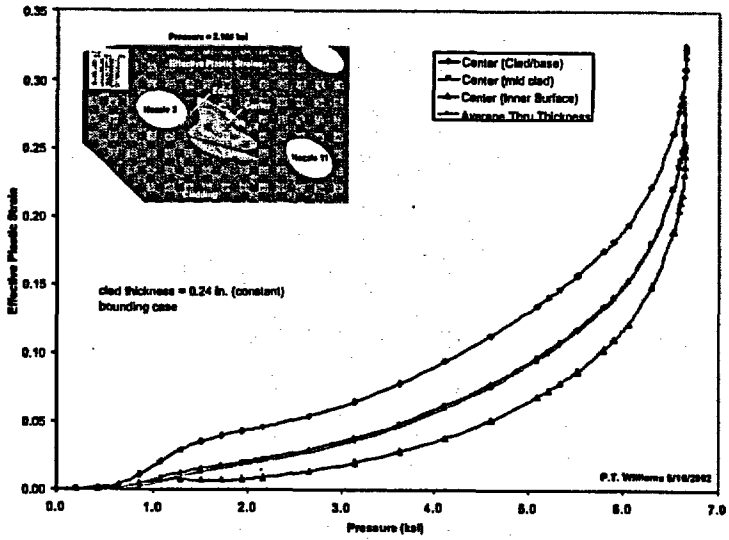

(a)

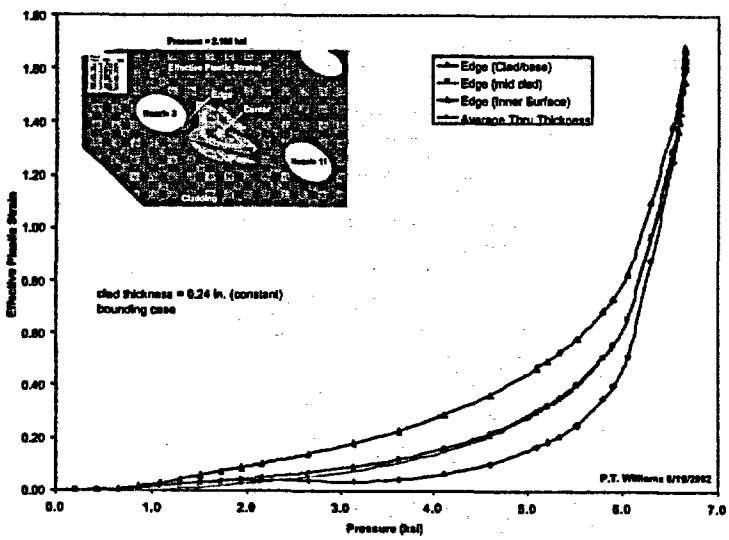

(b)

Fig. 12. Effective plastic-strain histories at two high-strain locations in the wastage area: (a) near the center and (b) near Nozzle 3.

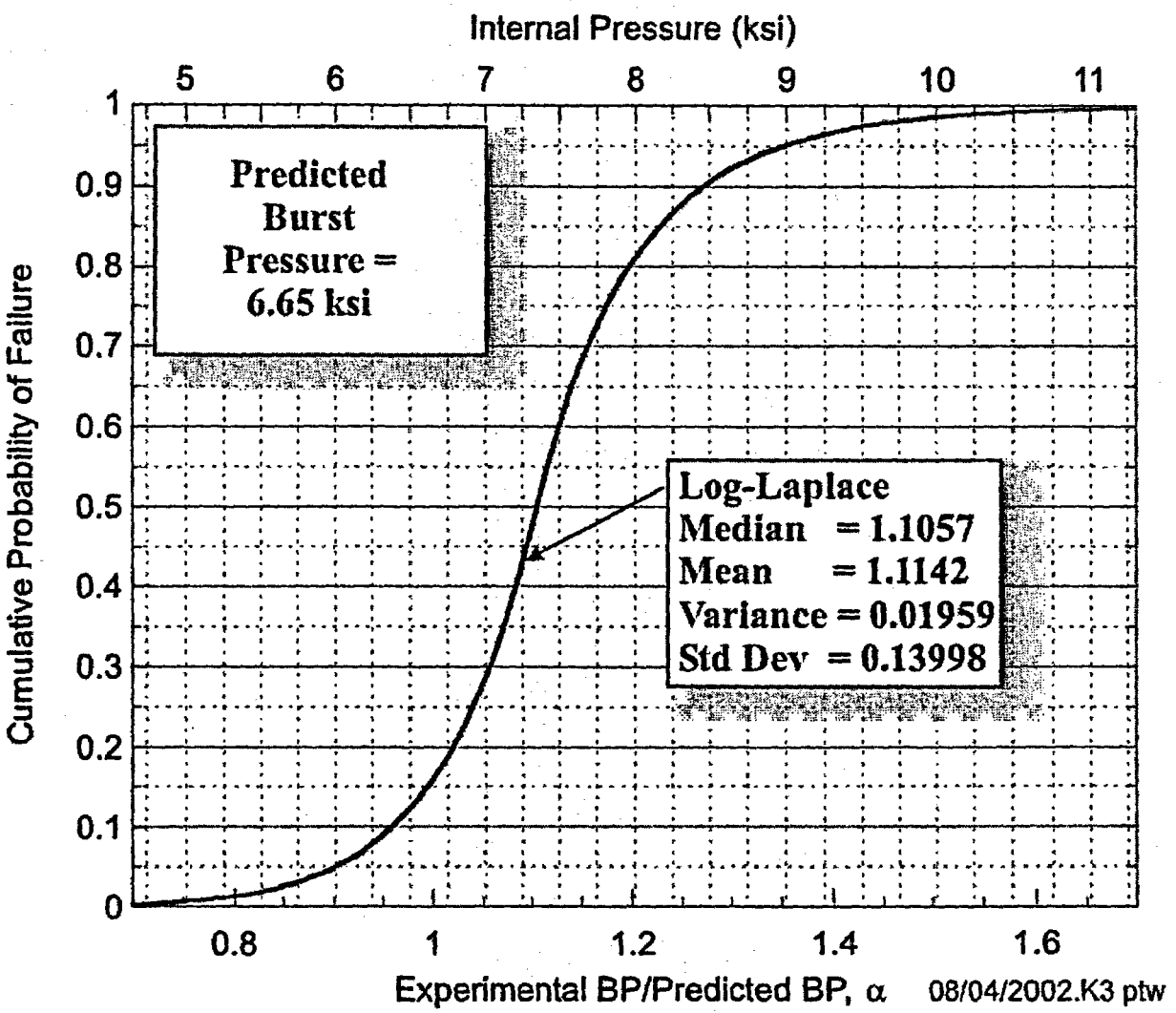

Fig. 13. Application of the failure statistical criterion produces a cumulative probability of failure (based on a Log-Laplace distribution) curve for the Bounding Case condition. Cumulative probability of failure as a function of internal pressure.

As discussed above, the bounding calculation predicted a burst pressure of 6.65 ksi which has a cumulative probability of failure of 0.158 for the Log-Laplace model. The Log-Laplace stochastic model also estimates a cumulative probability of failure of 4.14×10^{-7} at the operating pressure of 2.165 ksi and 2.15×10^{-6} at the set-point pressure of 2.5 ksi. See Table 11 for additional estimates from all six models. For the six distributions in Tables 8 and 11, the average probability of failure is 6.91×10^{-8} at 2.165 ksi, 3.60×10^{-7} at 2.5 ksi, and 0.2155 at 6.65 ksi.

Table 11. Estimated Cumulative Probability of Failures for the Bounding Calculation

Distribution	Parameters	Point Estimator	Parameter Values	Relative Score	Failure Probability at Internal Pressure		
					2.165 ksi	2.5 ksi	6.65 ksi
Log-Laplace	Location	Default	0	98	4.14E-07	2.15E-06	0.1582
	Scale	ML estimate	1.1057				
	Shape	ML estimate	11.45441				
Beta	Lower endpoint	MOM estimate	0.61449	93	0	0	0.2340
	Upper endpoint	MOM estimate	1.78866				
	Shape #1	MOM estimate	7.95564				
	Shape #2	MOM estimate	11.38552				
Gamma	Location	Default	0	89	8.17E-19	1.50E-15	0.2236
	Scale	ML estimate	0.01444				
	Shape	ML estimate	76.01293				
Normal	Mean	ML estimate	1.09747	83.33	8.44E-10	8.90E-09	0.2234
	Standard Dev.	ML estimate	0.12811				
Random Walk	Location	Default	0	75	0	0	0.2269
	Scale	ML estimate	0.92335				
	Shape	ML estimate	69.18788				
Inverse Gaussian	Location	Default	0	71	4.01E-29	1.79E-22	0.2269
	Scale	ML estimate	1.09747				
	Shape	ML estimate	82.23451				
				Average=	6.91E-08	3.60E-07	0.2155
				Standard Deviation=	1.69E-07	8.77E-07	0.0283

5. Summary and Conclusions

Six stochastic models of the probability of failure associated with a computational prediction of the plastic collapse of the exposed cladding in the wastage area of the Davis-Besse RPV head have been developed from the following technical bases:

(5) *experimental data* obtained during disk-burst tests reported by Riccardella [2] with loadings, geometries, and materials relevant to the Davis-Besse pressure loading, wastage-area footprint, and cladding,

(6) nonlinear, large-deformation, elastic-plastic *discrete-element analyses* of the disk-burst tests also reported in [2] (GAPL-3 discrete-element code[3]),

(7) nonlinear, finite-strain, elastic-plastic *finite-element analyses* performed for the current study (ABAQUS finite-element code[4]) of the nine disk-burst test specimens reported in [2], and

(8) a *theoretical criterion* for plastic instability in a circular diaphragm under pressure loading, due to Hill [5] (as cited in [6]), applied to the disk-burst tests.

Among the twenty-seven continuous distributions investigated, six passed all of the heuristic and *Goodness of Fit* tests applied in the analysis. The six distributions ranked in relative order are: (1) Log-Laplace, (2) Beta, (3) Gamma, (4) Normal, (5) Random Walk, and (6) Inverse Gaussian (Wald). As an example of how the stochastic models may be applied to the Davis-Besse wastage area problem, the top-ranked Log-Laplace model has the scaled form of

$$\Pr\left[P_{BP(true)} \le SP\right] = F_{LP}(SP \mid P_{BP}) = \begin{cases} \dfrac{1}{2}\left(\dfrac{SP}{1.1057 \times P_{BP}}\right)^{11.45441} & ; 0 < SP < 1.1057 \times P_{BP} \\ 1 - \dfrac{1}{2}\left(\dfrac{SP}{1.1057 \times P_{BP}}\right)^{-11.45441} & ; SP \ge 1.1057 \times P_{BP} \end{cases} \tag{27}$$

Given a computationally predicted burst pressure, P_{BP}, and service pressure, SP, the model gives an estimate of the cumulative probability of nonexceedance of the true but unknown burst pressure, $P_{BP(true)}$, i.e., $\Pr\left[P_{BP(true)} \le SP\right]$.

As an example application, estimates are provided for a bounding calculation of the "as-found" Davis-Besse wastage area. The bounding calculation predicted a burst pressure of 6.65 ksi which has a cumulative probability of failure of 0.158 by the Log-Laplace model. The Log-Laplace stochastic model also estimates a cumulative probability of failure of 4.14×10^{-7} at the operating pressure of 2.165 ksi and

2.15×10^{-6} at the set-point pressure of 2.5 ksi. For all six distributions, the average probability of failure is 6.91×10^{-8} at 2.165 ksi, 3.60×10^{-7} at 2.5 ksi, and 0.2155 at 6.65 ksi.

References

1. *Recent Experience with Degradation of Reactor Pressure Vessel Head,* NRC Information Notice 2002-11, United States Nuclear Regulatory Commission, Office of Nuclear Reactor Regulation, Washington, DC, March 12, 2002.
2. P. C. Riccardella, "Elasto-Plastic Analysis of Constrained Disk Burst Tests," Paper No. 72-PVP-12, presented at the ASME *Pressure Vessels and Piping Conference*, September 17-21, 1972, New Orleans, LA.
3. A. L. Thurman, *GAPL-3-A Computer Program for the Inelastic Large Deflection Stress Analysis of a Thin Plate or Axially Symmetric Shell with Pressure Loading and Deflection Restraints*, WAPD-TM-791, Bettis Atomic Power Laboratory, Pittsburgh, PA, June 1969.
4. *ABAQUS/Standard User's Manual, v. 6.2,* Hibbit, Karlsson, and Sorensen, Inc., Pawtucket, RI, 2001.
5. R. Hill, "A Theory of the Plastic Bulging of a Metal Diaphragm by Lateral Pressure," *Philos. Mag. (Ser. 7)* **41**, (1950) 1133.
6. A. R. Ragab and S. E. Bayoumi, *Engineering Solid Mechanics, Fundamentals and Applications*, CRC Press LLC, Boca Raton, FL, 1999.
7. W. E. Cooper, E. H. Kotteamp, and G. A. Spiering, "Experimental Effort on Bursting of Constrained Disks as Related to the Effective Utilization of Yield Strength," Paper No. 71-PVP-49, ASME *Pressure Vessels and Piping Conference*, May 1971.
8. J. Chakrabarty and J. M. Alexander, "Hydrostatic Bulging of Circular Diaphragms," *J. Strain Anal.* 5(3), (1970) 155-161.
9. A. M. Law, *Expert Fit© User's Guide*, Averill M. Law & Associates, Tuscon, Arizona, May 2002.
10. S. A. Loehlein, *Root Cause Analysis Report, Significant Degradation of Reactor Pressure Vessel Head,* CR 2002-0891, Davis-Besse Power Station, April 15, 2002.